Precambrian Research 385 (2023) 106947

Contents lists available at ScienceDirect

Precambrian Research

journal homepage: www.elsevier.com/locate/precamres

A DOM regulation model for dolomite versus calcite precipitation in the Ediacaran ocean: Implications for the "dolomite problem"

Wei Wang [a], Chao Li [b,c,d,*], Matthew S. Dodd [b,c,d], Thomas J. Algeo [a,e,f], Zihu Zhang [b,c,d], Meng Cheng [b,c,d], Mingcai Hou [b,c]

[a] State Key Laboratory of Biogeology and Environmental Geology, China University of Geosciences, Wuhan 430074, China
[b] State Key Laboratory of Oil and Gas Reservoir Geology and Exploitation & Institute of Sedimentary Geology, Chengdu University of Technology, Chengdu 610059, China
[c] Key Laboratory of Deep-time Geography and Environment Reconstruction and Applications of Ministry of Natural Resources, Chengdu University of Technology, Chengdu 610059, China
[d] International Center for Sedimentary Geochemistry and Biogeochemistry Research, Chengdu University of Technology, Chengdu 610059, China
[e] State Key Laboratory of Geological Processes and Mineral Resources, China University of Geosciences, Wuhan 430074, China
[f] Department of Geosciences, University of Cincinnati, Cincinnati, OH 45221-0013, USA

ARTICLE INFO

Keywords:
Doushantuo Formation
Shuram Excursion
Carbon isotopes
Dissolved organic matter
Ocean stratification
DOUNCE

ABSTRACT

The Ediacaran Period (~635–539 Ma) witnessed the largest negative carbonate carbon isotope ($\delta^{13}C_{carb}$) excursion in Earth history (to −12‰ VPDB), known as the Shuram Excursion (SE), which has been attributed to oxidation of a massive dissolved organic matter (DOM) reservoir, yielding highly ^{13}C-depleted oceanic dissolved inorganic carbon (DIC). Limestone and dolostone are intimately interbedded in the Ediacaran Doushantuo Formation (South China) as well as in coeval successions globally, suggesting frequent shifts between calcite and dolomite precipitation in the Ediacaran ocean. In this study, we compiled paired Mg/(Mg + Ca) and $\delta^{13}C_{carb}$ data for 991 well-preserved (i.e., minimally altered) carbonate-rich samples from 17 SE-associated sections with a wide global distribution. $\delta^{13}C_{carb}$ compositions vary among the dolomite-dominated (−10‰ to +7‰), calcite-dominated (mainly in −10‰ to −5‰), and mineralogically mixed samples (with a bimodal distribution of −10‰ to −5‰ or +4‰ to +8‰). Inspired by the recent DOM catalyzation hypothesis and the highly-stratified redox model as well as the large DOM reservoir hypothesis for the Ediacaran ocean, we propose a "DOM regulation model" to account for controls on the precipitation of dolomite versus calcite in the Ediacaran ocean and, thus, for observed Mg/(Mg + Ca)-$\delta^{13}C_{carb}$ patterns. In this model, calcite was precipitated under low-DOM conditions, which existed in oxic surface waters and the nearshore part of a mid-depth DOM-anaerobic oxidation zone. The former had $\delta^{13}C_{DIC} > +4‰$, buffered by atmospheric CO_2, whereas the latter had $\delta^{13}C_{DIC}$ decreasing from +4‰ to −10‰ due to increasing contributions of DOM oxidation. On the other hand, dolomite precipitation was catalyzed by high-DOM conditions, which existed in distal anoxic deep waters and the offshore part of the DOM-anaerobic oxidation zone. The former had $\delta^{13}C_{DIC} > +4‰$, ultimately buffered by atmospheric CO_2, whereas the latter had $\delta^{13}C_{DIC}$ increasing from −10‰ to +4‰ due to decreasing contributions of DOM oxidation. Our model is well supported by coexisting redox data. Our study highlights a possible link between massive dolomite formation and the existence of a large DOM reservoir in the Ediacaran ocean, providing an alternative perspective on the origin and widespread distribution of dolomite in deep-time marine systems (i.e., the "dolomite problem").

Abbreviations: $\delta^{13}C_{carb}$, carbonate carbon isotope; SE, Shuram Excursion; DOM, dissolved organic matter; DIC, dissolved inorganic carbon; POM, particulate organic matter; DOUNCE, Doushantuo Negative Carbon isotope Excursion; XRD, X-ray diffraction; $\delta^{18}O_{carb}$, carbonate fraction-based O-isotopes; CAS, carbonate-associated sulfate; $\delta^{13}C_{org}$, organic fraction-based C-isotopes; TOC, bulk-rock total organic carbon; IRMS, isotope ratio mass spectrometer; VPDB, Vienna Pee Dee belemnite; REE, rare earth elements; PAAS, Post Archean Australian Shale; Δ_{47}, clumped-isotope; CCD, carbonate compensation depth; DIC_{ox}, DIC from local DOM oxidation; DIC_{bg}, background DIC; PAL, present atmospheric level; MSR, microbial sulfate reduction.

* Corresponding author at: State Key Laboratory of Oil and Gas Reservoir Geology and Exploitation & Institute of Sedimentary Geology, Chengdu University of Technology, Chengdu 610059, China.
E-mail address: chaoli@cdut.edu.cn (C. Li).

https://doi.org/10.1016/j.precamres.2022.106947
Received 26 July 2022; Received in revised form 9 December 2022; Accepted 10 December 2022

1. Introduction

Dolomite (i.e., calcium magnesium carbonate, $CaMg(CO_3)_2$) is one of the most common mineral components in marine successions throughout Earth history, with Precambrian strata having a particularly high proportion of dolostone relative to limestone. On the other hand, dolomite is scarce in modern sedimentary environments—an observation that is puzzling in view of the supersaturation of the modern ocean with respect to dolomite. This paradox is known as the "dolomite problem", and it has been investigated for decades without resolution (e.g., Fairbridge, 1957; Hsü, 1966; Holland and Zimmerman, 2000; Warren, 2000; McKenzie and Vasconcelos, 2009; Gregg et al., 2015). The rarity of dolomite in modern shallow-marine facies can be attributed to the notorious difficulty (relative to calcite) of its precipitation under ambient Earth-surface conditions due to hydration effects, which can inhibit incorporation of Mg^{2+} into the dolomite crystal lattice or prevent boundary-layer Mg^{2+} from bonding with CO_3^{2-}, thereby hindering crystal growth (Lippmann, 1982; Mucci and Morse, 1983; Stephenson et al., 2008; Roberts et al., 2013; Shen et al., 2015; Qiu et al., 2017; Zhang et al., 2021; Fang et al., 2022). However, dolomite formation is observed in low-oxygen and low-sulfate modern environments, especially in association with organic decay and/or microbial activity (Dedeckker and Last, 1988; Vasconcelos and McKenzie, 1997; Wright, 1999; Warthmann et al., 2000; Liu et al., 2019). The prevalence of dolomite in Precambrian marine successions has been attributed to contemporaneous seawater having had a substantially different composition (e.g., $[Mg]^{2+}$, $[SO_4]^{2-}$), properties (e.g., alkalinity, redox), and/or microbial activity levels than Phanerozoic seawater, favoring the precipitation of dolomite as a primary or early secondary mineral phase (Petrash et al., 2017; Wood et al., 2017; Cantine et al., 2020; Chang et al., 2020; Wang et al., 2020).

Dissolved organic matter (DOM) is the largest reservoir of reduced carbon in the modern ocean (~662 Pg C), representing >100× the carbon inventory of total marine biomass (~6 Pg C) and an amount similar to the atmospheric CO_2 reservoir (~750 Pg C) but much smaller than the marine dissolved inorganic carbon (DIC) reservoir (~38,000 Pg C) (Hansell et al., 2009; Jiao et al., 2010; Ciais et al., 2013; Hansell, 2013; Bar-On et al., 2018). The concentration of DOM is ~45 μmol C/L in the deep global ocean but up to 120 μmol C/L in the Black Sea basin due to the low oxygen levels of the latter (Albert et al., 1995; Ducklow et al., 2007). In theory, more reducing conditions would have favored a larger seawater DOM inventory during periods of widespread oceanic anoxia, which subsequently may have been rapidly oxidized to DIC following re-establishment of oxic conditions (Ridgwell and Arndt, 2015; Gomez-Saez et al., 2021). Although multiple mechanisms can produce DOM, a major pathway is solubilization of particulate organic matter (POM) by bacterial and archaeal ectohydrolases (Nagata et al., 2000; Jiao et al., 2010). As determined by Fourier transform ion cyclotron resonance mass spectrometry and nuclear magnetic resonance, carboxyl-rich alicyclic molecules that are believed to be refractory to microbial breakdown are often the most abundant components of DOM in the deep ocean (Hertkorn et al., 2006; Zhang et al., 2018). Many studies have shown that dolomite crystallization is a kinetically controlled process (e.g., Baker and Kastner, 1981; Lippmann, 1982; Land, 1998; Urosevic et al., 2012; Shen et al., 2014; Wang et al., 2016a), and the hydration effect of Mg^{2+} has been recognized as a key kinetic barrier to the incorporation of Mg^{2+} into the lattice of dolomite (Zhang et al., 2012a, 2012b; Shen et al., 2014, 2015; Toroz et al., 2021). Recent advances in dolomite genesis have demonstrated that microbially-derived DOM can serve as a catalyst for formation of Mg-bearing calcites and even protodolomites (herein termed the "DOM catalyzation hypothesis"; e.g., Stephenson et al., 2008; Zhang et al., 2012b; Kenward et al., 2013; Roberts et al., 2013; Qiu et al., 2017; Petrash et al., 2017; Liu et al., 2020; Al Disi et al., 2021). This process is based on attachment of Mg-H_2O complexes to free carboxylic functional groups of DOM via electrostatic attraction, releasing a H_2O molecule and promoting formation of Mg-H_2O-carboxyl complexes (i.e., $[Mg(H_2O)_5(R\text{-}COO)]^+$), reducing the energy of carbonation and making incorporation of Mg^{2+} into the dolomite crystal lattice more thermodynamically favorable (Roberts et al., 2013). This pathway provides a possible mechanism for formation of massive dolomite in Precambrian oceans.

The Ediacaran Period (~635–539 Ma) was characterized by highly redox-stratified oceans with oxic conditions in shallow-shelf settings and anoxic conditions plus low sulfate concentrations (<2 mM) in deep waters (Li et al., 2010, 2020a; Loyd et al., 2012b; Fan et al., 2014; Kendall et al., 2015; Osburn et al., 2015; Sahoo et al., 2016). It also witnessed multiple negative carbonate carbon isotope excursions, including the largest excursion in Earth history (to −12‰ VPDB, from a pre-excursion value of > +5‰), which is known as the Shuram Excursion (SE) or the Doushantuo Negative Carbon isotope Excursion (DOUNCE). These $\delta^{13}C_{carb}$ excursions have been widely attributed to oxidation of a large DOM reservoir in the anoxic deep ocean and associated generation of isotopically light DIC (herein termed the "large DOM reservoir hypothesis"; e.g., Rothman et al., 2003; Fike et al., 2006; Jiang et al., 2007; Li et al., 2017; Shields et al., 2019; Chen et al., 2022; Xing et al., 2022). Considering the lack of production of zooplankton fecal pellets and siliceous skeletons (Logan et al., 1995), organic matter would have had a much longer residence time in the Precambrian oceanic water column. This condition would have allowed buildup of a large DOM reservoir in the Ediacaran ocean, possibly to 100–1000× the mass of that in the modern ocean based on geochemical modeling (Rothman et al., 2003). Limestone-dolostone transitions are common in the Doushantuo Formation (South China) as well as in age-equivalent successions globally, suggesting frequent shifts between calcite and dolomite precipitation in the Ediacaran ocean. Recent advances in understanding dolomite genesis support the hypothesis that microbially-generated DOM facilitated formation of Mg-bearing calcite and even protodolomite in the Ediacaran ocean (Chang et al., 2020), although further investigation of deep-time dolomite formations is needed.

In this study, we generated geochemical and X-ray diffraction (XRD) data for 5 Ediacaran carbonate-platform sections in South China (Zhangcunping, Xiangerwan, Jiulongwan, Zhongling and Siduping), and we compiled equivalent proxy data for another 12 Ediacaran carbonate sections with a wide global distribution and representing a range of depositional water depths. The geochemical dataset includes carbonate fraction-based C- and O-isotopes ($\delta^{13}C_{carb}$ and $\delta^{18}O_{carb}$), Mg/(Mg + Ca) [molar ratio], Mn/Sr, $\delta^{34}S_{CAS}$ (note: CAS = carbonate-associated sulfate), Ce/Ce* and I/(Ca + Mg), organic fraction-based C-isotopes ($\delta^{13}C_{org}$), and bulk-rock total organic carbon (TOC) data for a total of 991 well-preserved samples. The selected sections represent either the full SE interval or a large part thereof, and a number of them contain limestone-dolostone alternations. This dataset thus provides us a chance to test the validity of the two DOM-related hypotheses described above as well as examine paleoceanic chemistry within a specific temporal window of relevance to the "dolomite problem".

2. Data collection, sedimentary facies and data screening

Our dataset encompasses 17 sections of Ediacaran age from five regions across four paleocontinents (Fig. 1a), representing all currently available SE sections with published geochemical data, including six sections in South China (paleolatitudes of 8 ± 5 °N), four sections in southeastern Siberia (paleolatitudes of 17 ± 3 °N), one section in central Oman (paleolatitude of 27 ± 3 °S), one section in southwestern Mexico (paleolatitude of 0 ± 3 °N), and five sections in northwestern Canada (paleolatitudes of 9 ± 3 °N), the paleolatitudes of five study regions were estimated from Merdith et al. (2017). Thus, all sections were located in the paleo-tropics or -subtropics, within the latitudinal belt of carbonate precipitation (i.e., which is between ~30°N and ~30°S in the modern ocean) (Nelson, 1988).

All of the South China data are from the Doushantuo Formation (~635–551 Ma; Condon et al., 2005), in which several different depositional settings are represented, providing a proximal-to-distal (shelf-to-basin) transect across the Yangtze Platform: Zhangcunping (inner shelf, n = 106), Xiangerwan (intra-shelf basin, n = 84), Jiulongwan (intra-shelf basin, n = 70), Zhongling (shelf margin, n = 22), Daotuo (upper slope, n = 19) and Siduping (upper slope, n = 147) (Fig. 1b and 2; Jiang et al., 2011). Although various hypotheses have been proposed to explain the formation of cap dolostones (Member I of the Doushantuo Formation) in South China (e.g., Grotzinger and Knoll, 1995; Hoffman et al., 1998; James et al., 2001; Kennedy et al., 2001; Higgins and Schrag, 2003; Jiang et al., 2003; Wang et al., 2008; Kennedy and Christie-Blick, 2011; Wang et al., 2017), there is considerable debate about whether these sections record global signals or regional sedimentary and/or diagenetic processes (Lv et al., 2018; Wei et al., 2019a). Therefore, we did not include data from Member I in our dataset, and we limited our analysis to Members II to IV of the Doushantuo Formation. The Zhangcunping, Jiulongwan, Zhongling, Daotuo and Siduping sections were previously sampled and analyzed by Li et al. (2010, 2017), Wang et al. (2016b) and Wei et al. (2019b), and only the Xiangerwan section was newly collected for the present study. We measured Mg/(Mg + Ca) for all samples except for some from Jiulongwan, Siduping, and Daotuo, which were taken from Zhang et al. (2019), Wang et al. (2016b) and Wei et al. (2019b), respectively. We also measured $\delta^{13}C_{carb}$, $\delta^{18}O_{carb}$, $\delta^{13}C_{org}$, and TOC for the Xiangerwan section and $\delta^{13}C_{carb}$ and $\delta^{18}O_{carb}$ for the Zhongling section, whereas the remainder of the geochemical data was derived or calculated from published sources (Melezhik et al., 2009; Li et al., 2010, 2017, 2020b; Loyd et al., 2012b, 2013; Osburn, 2013; Wang et al., 2016b; Hardisty et al., 2017; Shi et al., 2018; Wei et al., 2019b; Zhang et al., 2019; Cao et al., 2020; Chang et al., 2020; Busch et al., 2022), as reported in detail in the Supplementary Information. We carried out XRD analyses of representative samples for all sections except Daotuo.

The southeastern Siberian samples (n = 151) are from the Nikol'skaya, Chenchinskaya (also known as Torginskaya or Alyanchskay), and Zherbinskaya (Kholychskaya) formations in the Chara (Fig. 3a, n = 57), Zhuya East (Fig. 3b, n = 28), Zhuya West (Fig. 3c, n = 16), and Bol'shoy Patom (Fig. 3d, n = 50) sections, which were deposited mainly on a shallow carbonate platform that was well connected to the open ocean and that was characterized neither by basinal isolation nor by chemical or physical stratification (see Melezhik et al., 2009 for details). All geochemical data were compiled from Melezhik et al. (2009) except for Ce/Ce* in the Bol'shoy Patom section, which are from Zhang et al. (2019).

The central Oman samples (Fig. 3e, n = 154) are from the Khufai, Shuram and Buah formations of the Nafun Group of the Huqf Supergroup in the Huqf area of the Sultanate of Oman. The so-called "Huqf section" is a compilation of data from outcrops within a relatively small area (~250 km^2), as reported in Hardisty et al. (2017). This section represents a shallow-marine setting on a carbonate ramp (see Osburn, 2013 for details). Geochemical data were compiled from Osburn (2013), Hardisty et al. (2017), and Busch et al. (2022).

The southwestern Mexican samples (Fig. 3f, n = 21) are from the Clemente, Gamuza and Papalote formations of the "Sonora Succession" in the Cerro Rajón section, which is located ~30 km southeast of the town of Caborca, in Sonora State, northwestern Mexico. The Sonora Succession accumulated in a predominantly shallow-marine setting (Stewart et al., 1984). Geochemical data were compiled from Loyd et al. (2012b, 2013), Hardisty et al. (2017) and Li et al. (2020b).

The northwestern Canadian samples (n = 217) are from the Gametrail Formation (JB1713 in Goz B, Fig. 3g, middle ramp, n = 62; JB1822 in Goz C, Fig. 3h, outer ramp, n = 58) in the Goz Creek area of the Wernecke Mountains of eastern Yukon and from the Last Chance Formation (JB1704/J1711, Fig. 3i, n = 46; JB1705, Fig. 3j, n = 31; JB1807, Fig. 3k, outer ramp, n = 20) in the Coal Creek area of the Ogilvie Mountains of western Yukon (Busch, 2022). Geochemical data were compiled from Busch et al. (2022).

A detailed description of the geological settings of the study sections and data sources are provided in the Supplementary Information. The dataset used in this study was prescreened to eliminate potentially problematic samples. In generating geochemical data, we avoided the effects of diagenetic or secondary alteration on Mg/(Mg + Ca) and $\delta^{13}C_{carb}$ values by analyzing only microcrystalline carbonates, which are likely to represent primary carbonate precipitates, and we removed any weathered surfaces, secondary veins and cements prior to sample powdering. In compiling geochemical data, we applied multiple screening methods to limit the influence of burial-stage authigenic carbonates that may record secondary (diagenetic) signatures and made use of data only from samples that are likely to represent primary carbonate precipitates (Table S1). First, we collected data only from

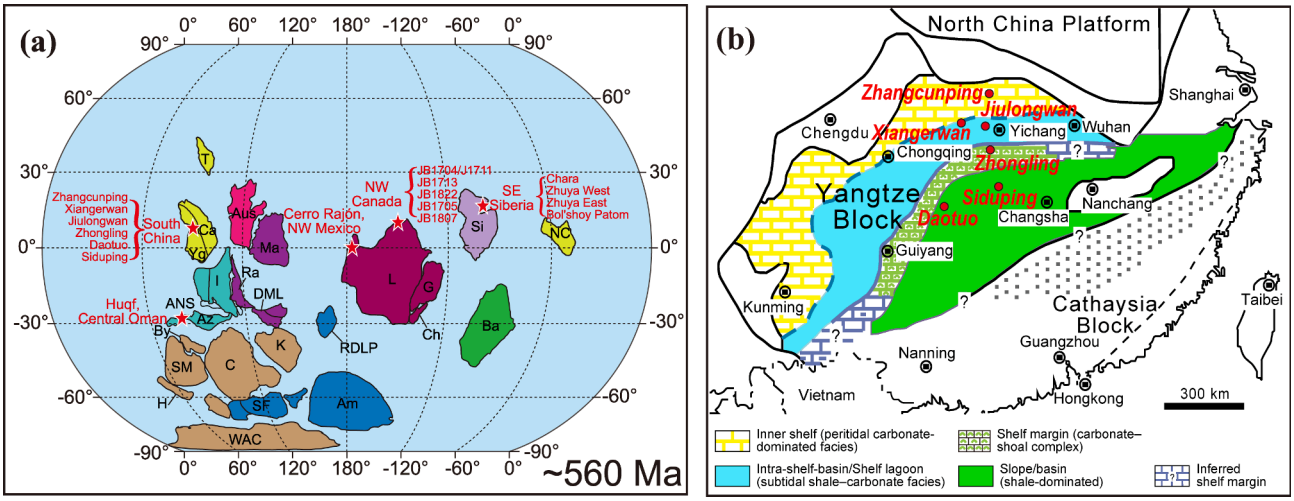

Fig. 1. Geological map of study regions. (a) Paleogeography at ~560 Ma (modified after Merdith et al., 2017). The study regions are indicated by red stars. Abbreviations: Am, Amazonia; ANS, Arabian-Nubian Shield; Aus, Australia; Az, Azania; Ba, Baltica; By, Bayuda; C, Congo; Ca, Cathaysia (South China); Ch, Chortis; DML, Dronning Maud Land; G, Greenland; H, Hoggar; I, India; K, Kalahari; L, Laurentia; Ma, Mawson; NC, North China; Ra, Rayner (Antarctica); RDLP, Rio de la Plata; SF, São Francisco; Si, Siberia; SM, Sahara Metacraton; T, Tarim; WAC, West African Craton; Yg, Yangtze Craton (South China). (b) Paleogeographic reconstruction of the Ediacaran Yangtze Platform (modified after Jiang et al., 2011; Li et al., 2017) showing locations of the six study sections in South China (Zhangcunping, Xiangerwan, Jiulongwan, Zhongling, Daotuo and Siduping).

samples with a carbonate mineral content (calculated from Ca and Mg concentrations) of >50%. In some studies, where Mg and Ca concentrations were not given (e.g., Loyd et al., 2013; Wang et al., 2016b; Hardisty et al., 2017; Busch et al., 2022), we relied on lithologic descriptions in the source publication, limiting our analysis to samples that were designated as limestone or dolostone. Second, because strong post-depositional (diagenetic) alteration of marine carbonate rocks commonly results in elevated Mn/Sr ratios and a decrease in $\delta^{18}O_{carb}$ (Kaufman and Knoll, 1995; Knauth and Kennedy, 2009), we screened out samples with Mn/Sr > 10 or $\delta^{18}O_{carb}$ < −10‰. Third, because fluorapatite can release Ca during acid hydrolysis, resulting in reduced Mg/(Mg + Ca) values, we selected representative samples of each section for XRD analysis to remove samples influenced by fluorapatite. A total of 991 samples in our dataset passed these screening criteria. Several formations (e.g., the Wonoka Formation in South Australia, Zhang et al., 2019, Busch et al., 2022; the Johnnie Formation in Death Valley region, southwestern USA, Hardisty et al., 2017, Busch et al., 2022) were excluded in their entirety from our dataset owing to a large majority of their samples failing to meet the screening criteria. The primary nature of Ce/Ce* signals used in evaluation of redox conditions had been tested in the source publications (e.g., Zhang et al., 2019 for the Jiulongwan and Bol'shoy Patom sections; Cao et al., 2020 for the Siduping section; and Chang et al., 2020 for the Zhangcunping section).

3. Experimental methods

Large samples (>200 g) of the Doushantuo Formation were carefully trimmed to remove possible weathered surfaces, post-depositional veins and any visible pyrite nodules or bands, and then cut into small pieces. The freshest pieces were chosen and crushed to powder (>200 mesh) before undertaking the geochemical and XRD analyses of this study. All of the following analyses were conducted at the China University of Geosciences-Wuhan.

To measure Mg and Ca contents of the carbonate fraction of a sample, an aliquot of 10 mg of rock powder was digested in 10 mL of 2% analytical-grade HNO_3 at room temperature for 48 h with agitation. This treatment specifically releases Mg and Ca from the carbonate fraction of the sample (Loyd et al., 2013). After centrifugation, about 1 mL of supernatant was extracted and then diluted with 9 mL of 2% analytical-grade HNO_3 for Ca-Mg measurements either on an inductively coupled plasma-optical emission spectrometer (EXPEC 6000, Puyu) or an inductively coupled plasma-atomic emission spectroscopy (IRIS Intrepid II XSP, Thermo Electron). Ca and Mg contents are reported in weight percent (wt.%) and the analytical precision is better than ±1% of reported values based on replicate analyses.

$\delta^{13}C_{carb}$ and $\delta^{18}O_{carb}$ were measured on an isotope ratio mass spectrometer (IRMS) (MAT253, Thermo Fisher Scientific). Approximately 60–300 μg of homogenized sample powder were loaded into a vial. The sample was then reacted with 100% H_3PO_4 under a vacuum at 70 °C for 220 s using a Kiel IV device. The produced CO_2 was subsequently introduced into the IRMS for isotopic measurements. All carbon and oxygen isotope data for carbonates are reported in per mille (‰) relative to the Vienna Pee Dee belemnite (VPDB) standard with a precision better than ± 0.1‰ (1σ) based on multiple analyses of national and laboratory standards (GBW04416, $\delta^{13}C_{carb}$ = +1.61‰, $\delta^{18}O_{carb}$ = −11.59‰; GBW04417, $\delta^{13}C_{carb}$ = −6.06‰, $\delta^{18}O_{carb}$ = −24.12‰; and internal standard, ISTB-1, $\delta^{13}C_{carb}$ = −10.63‰, $\delta^{18}O_{carb}$ = −8.63‰).

An aliquot of sample powder (~3 g) was first treated with 4 M HCl to remove inorganic carbon, thoroughly rinsed to neutral pH, then centrifuged and dried at 60 °C for 24 h. The residues were used for $\delta^{13}C_{org}$ and TOC measurements. $\delta^{13}C_{org}$ was measured online using a Flash EA 2000 interfaced with a MAT 253 IRMS and calibrated with glycine (δ^{13} = –33.3%) and collagen (δ^{13} = –9.0%) SIGMA standards. Results are reported relative to the VPDB standard with a precision better than ±0.2‰ based on duplicated analyses of study samples.

TOC was measured by combustion of the residues in a 902T C-S analyzer (Beijing Wanliandaxinke Instruments Co. Ltd) with a detection limit is 0.01%. Results are reported with a precision better than ±0.5% (1σ) based on replicate analyses of Alpha Resources standard AR4007 (total carbon: 7.27%).

XRD analysis was carried out on a Dandong Tongda TD-3500 X-ray diffractometer using Cu Kα radiation at 40 kV and 30 mA, with a 2θ range of 3° to 65° and a step size of 0.02/s.

4. Results

The geochemical data compiled in this study are shown in Figs. 2-8 and Table S1. All 17 of the selected study sections record the SE in whole or in part, and a number of them contain limestone-dolostone alternations (Figs. 2 and 3).

Ca-Mg carbonate minerals are customarily categorized as low-Mg calcite (<4 mol.% $MgCO_3$, molar ratio), high-Mg calcite (4–36 mol.% $MgCO_3$), and dolomite (36–55 mol.% $MgCO_3$, including disordered dolomite and protodolomite) (Gregg et al., 2015; Fang and Xu, 2019; Fang et al., 2022). Many primary carbonate minerals are metastable phases, with high-Mg calcite (and aragonite) transforming to low-Mg calcite and disordered dolomite and protodolomite to ordered dolomite during burial diagenesis (Tucker and Wright, 1990; Burton, 1993; Nordeng and Sibley, 1994; Gregg et al., 2015; Pina et al., 2022), resulting in carbonate rocks in deep-time systems being composed mainly or exclusively of low-Mg calcite and ordered dolomite. For the sake of simplicity, primary low-Mg calcite and high-Mg calcite are collectively referred to as "calcite" in samples, and primary disordered dolomite and protodolomite as "dolomite" in samples. In order to better describe the mineralogic character of the study samples, customary Mg/(Mg + Ca) ranges of <0.04, 0.04–0.36, and 0.36–0.55 as above were used for assignment to one of three categories: calcite-dominated samples, mineralogically mixed samples (in which both calcite and dolomite are present in substantial amounts; henceforth, "mixed samples"), and dolomite-dominated samples, respectively (Fig. 4).

4.1. $\delta^{13}C_{carb}$ vs Mg/(Mg + Ca)

Distinct relationships between $\delta^{13}C_{carb}$ and Mg/(Mg + Ca) are evident for 6 sections in South China (Fig. 4a) and all 17 sections available globally (Fig. 4b). As shown in Fig. 4b, the dolomite-dominated samples comprise the bulk of our dataset [709 of 991 samples, or 70.4%, including 11 samples with Mg/(Mg + Ca) values a slightly greater than 0.55, most likely due to imprecise test], and they include both SE and non-SE samples exhibiting $\delta^{13}C_{carb}$ values ranging from about −10‰ to +7‰ with a statistically non-significant relationship to Mg/(Mg + Ca) (n = 709, r = +0.04, $p \gg 0.10$). The calcite-dominated samples (166 of 991 samples, or 16.8%) are almost entirely associated with large negative $\delta^{13}C_{carb}$ excursions (<−5‰, 160 samples) of Ediacaran age, with just 6 samples having $\delta^{13}C_{carb}$ values from about −3‰ to +4‰. The mixed samples (116 of 991 samples, or 11.7%) exhibit a bimodal distribution with $\delta^{13}C_{carb}$ either −10‰ to −5‰ (80 samples) or +4‰ to +8‰ (29 samples), with just 7 samples having $\delta^{13}C_{carb}$ values between −5‰ and +4‰. We divided the Fig. 4 crossplots into five fields (labeled Modes 1 to 5 with subfields 1a and 1b for Mode 1, subfields 2a, 2b and 2c for Mode 2, and subfields 4a and 4b for Mode 4) mostly based on the key thresholds of 0.04, 0.36 and 0.55 for the Mg/(Mg + Ca) axis and –5‰ and +4‰ for the $\delta^{13}C_{carb}$ axis (note: subfield 4a is specifically defined by a transitional zone between Mode 3 and Mode 4b). The distribution of samples among the five modes is shown in Fig. 4c, with just 14 out of 991 samples (1.4%) not falling within one of these modes and likely due to imprecise test. Mode 2 (i.e., samples with $\delta^{13}C_{carb}$ < −5‰; n = 388) contains samples from all three mineralogic categories [i.e., calcite-dominated (Mode 2a); mixed (Mode 2b); dolomite-dominated (Mode 2c)], whereas the other modes (which have n ranging from 6 to 456) each contain just one mineralogic category (Fig. 4c).

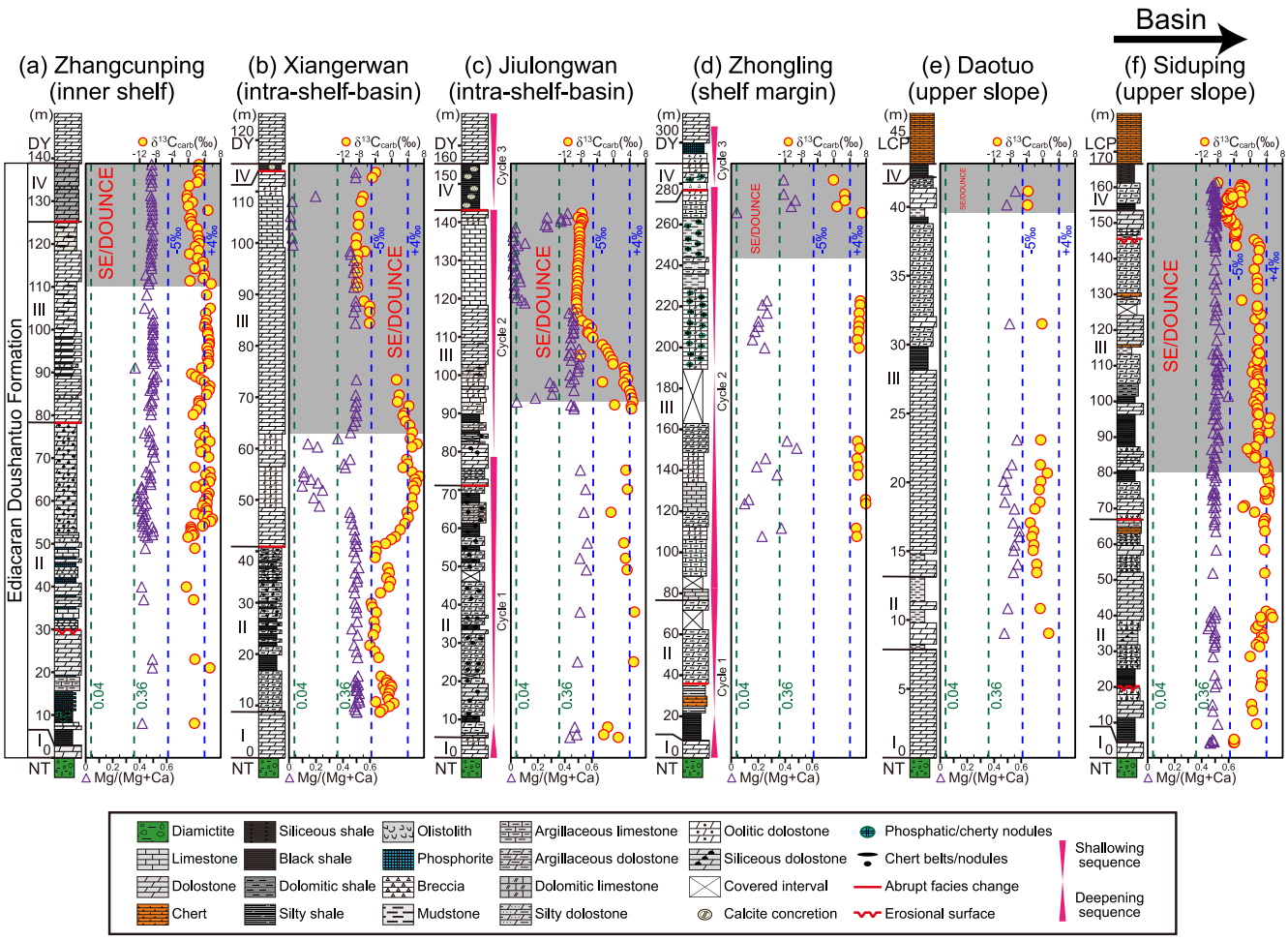

Fig. 2. Mg/(Mg + Ca) and $\delta^{13}C_{carb}$ profiles of the 6 study sections (a, Zhangcunping; b, Xiangerwan; c, Jiulongwan; d, Zhongling; e, Daotuo; f, Siduping) in South China with the direction from proximal to distal across the Yangtze Platform. The sedimentary cycle data of the Jiulongwan and Zhongling section are adopted from McFadden et al. (2008) and Zhu et al. (2007) respectively. Gray areas represent Shuram Excursion (SE). Abbreviations: NT, Nantuo Formation; DY, Dengying Formation; LCP, Liuchapo Formation. Detailed data sources are listed in Table S1.

4.2. XRD results of representative samples

XRD analysis was undertaken on 55 samples representing all modes except Mode 1 (for which samples are unavailable). The mineralogic composition of most samples is limited to dolomite, calcite and quartz, whose proportions differ among the study samples (Fig. 5). Only small amounts of fluorapatite (<10 wt% of carbonate minerals based on semi-quantitative calculations from XRD data; Fig. 5b, d) are present in some samples from the Zhangcunping (named "ZK312-" or "P312-") and Zhongling (named "SH-") sections, demonstrating that Mg/(Mg + Ca) values are not markedly affected by fluorapatite. The carbonate minerals in Mode 2 change from mainly calcite (Mode 2a) to mixed (Mode 2b) to mainly dolomite (Mode 2c) with increases in Mg/(Mg + Ca) (Fig. 5a). Modes 3 and 5 contain almost exclusively dolomite (Fig. 5b, d), and Mode 4 contains mixed carbonate minerals (Fig. 5c).

4.3. $\delta^{13}C_{carb}$, $\delta^{13}C_{org}$ and $\Delta^{13}C_{carb\text{-}org}$

$\delta^{13}C_{carb}$, $\delta^{13}C_{org}$ and $\Delta^{13}C_{carb\text{-}org}$ (i.e., $\delta^{13}C_{carb} - \delta^{13}C_{org}$) exhibit distinct relationships in the study sections (Fig. 6). $\delta^{13}C_{carb}$ values vary from −9.10‰ to + 6.89‰ (−0.50‰ to +5.60‰ for Zhangcunping, −8.78‰ to +6.89‰ for Xiangerwan, −9.10‰ to +5.20‰ for Jiulongwan and −8.00‰ to + 5.50‰ for Siduping). Although the $\delta^{13}C_{carb}$ profiles for all sections show large fluctuations (i.e., Zhangcunping varies from –0.5‰ to + 5.9‰, and the other three sections from <–8‰ to > +5‰), nearly all $\delta^{13}C_{org}$ values at Zhangcunping (53 of 56 samples) and Xiangerwan (82 of 84 samples), most $\delta^{13}C_{org}$ values at Siduping (113 of 143 samples), and more than half of $\delta^{13}C_{org}$ values at Jiulongwan (34 of 63 sample) vary within the narrow range of –30‰ to –25‰ (Figs. 6 and 7a). The remaining samples are largely in accord with the middle-late stage of the SE (e.g., ~118–142 m at Jiulongwan, and ~150–161 m at Siduping). Contrary to $\delta^{13}C_{org}$ (which is decoupled from $\delta^{13}C_{carb}$), the $\Delta^{13}C_{carb\text{-}org}$ profiles show a clear correlation with $\delta^{13}C_{carb}$ (Fig. 7b), and there is no correlation between $\Delta^{13}C_{carb\text{-}org}$ and $\delta^{13}C_{org}$ for any section when considered over its full thickness, except for a weak correlation at Zhangcunping (Fig. 7c); however, some intervals of the Jiulongwan and Siduping sections (especially those with $\delta^{13}C_{org}$ < −30‰) show a clear negative correlation between $\Delta^{13}C_{carb\text{-}org}$ and $\delta^{13}C_{org}$. These local negative correlations are associated with the middle to late stages of the SE (Fig. 6c, d).

4.4. TOC

Most samples in all four sections have TOC lower than 0.5% (41 of 59 samples at Zhangcunping, 55 of 84 samples at Xiangerwan, 41 of 68 samples at Jiulongwan, and 141 of 143 samples at Siduping) (Fig. 6). There is no correlation between $\Delta^{13}C_{carb\text{-}org}$ and $\delta^{13}C_{org}$ at Xiangerwan ($n = 84$, $r = -0.02$, $p > 0.10$) and Siduping ($n = 143$, $r = -0.12$, $p > 0.10$), but weak correlations exist in the Zhangcunping ($n = 59$, $r = +0.29$, $p < 0.05$) and Jiulongwan sections ($n = 68$, $r = +0.23$, $p < 0.10$) (Fig. 7d).

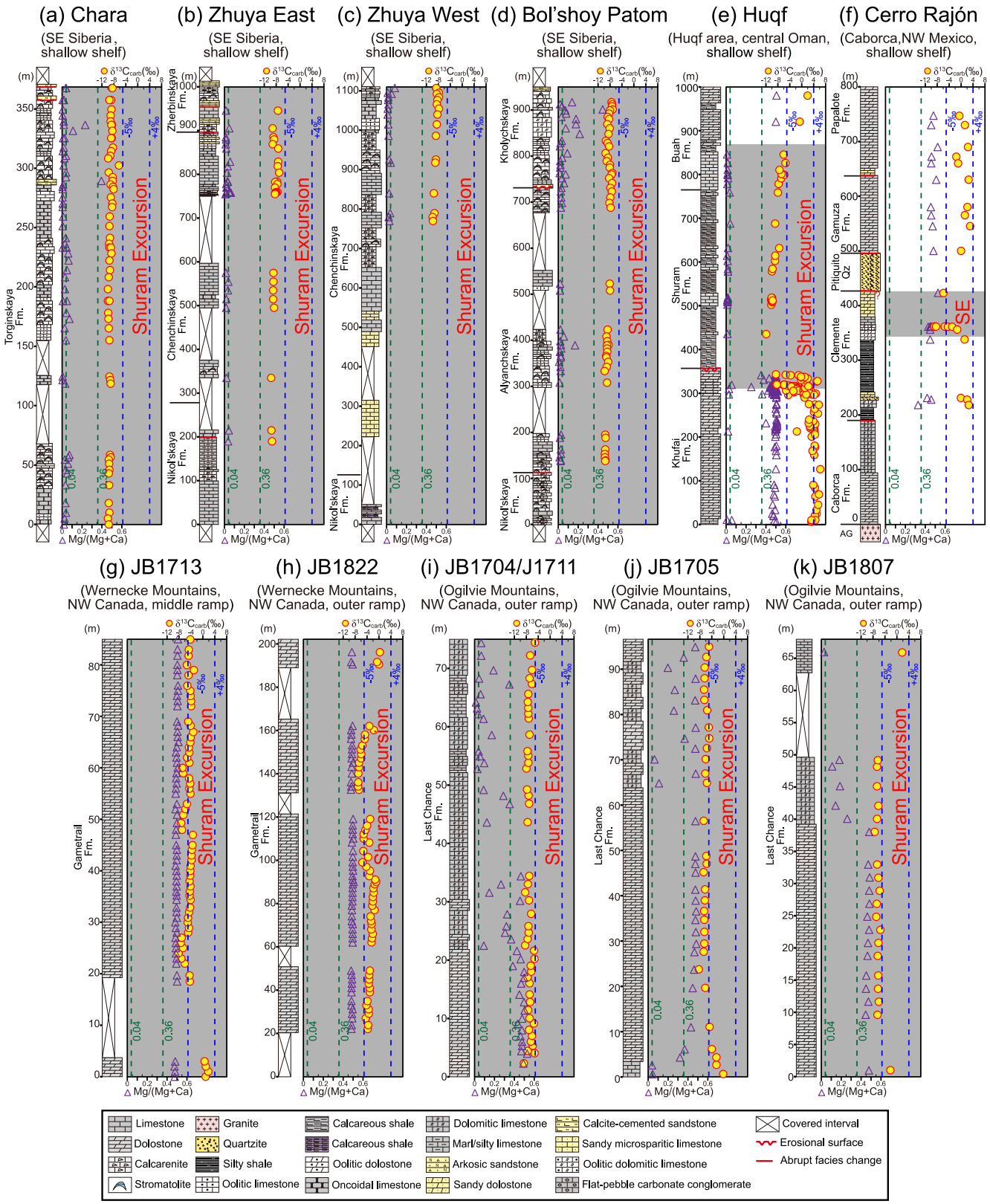

Fig. 3. Mg/(Mg + Ca) and $\delta^{13}C_{carb}$ profiles of the 11 study sections (a, b, c, d in southeastern Siberia; e in central Oman; f in southwestern Mexico; g, h, i, j, k in northwestern Canada) from other localities than South China. Abbreviations: Fm., Formation; AG, Aibo Granite. Detailed data sources are listed in Table S1.

4.5. $\delta^{34}S_{CAS}$

$\delta^{34}S_{CAS}$ values vary from + 0.7‰ to + 60.1‰ (Fig. 8a, +7.5‰ to +44.0‰ for Jiulongwan, +30.5‰ to +60.1‰ for Zhongling, +0.7‰ to +47.6‰ for Siduping, +18.8‰ to +40.5‰ for Huqf and +18.9‰ to +32.3‰ for Cerro Rajón). $\delta^{34}S_{CAS}$ shows a moderate positive correlation with $\delta^{13}C_{carb}$ in the four study sections ($n = 124$, $r = +0.50$, $p < 0.01$), with stronger relationships for Jiulongwan ($n = 32$, $r = +0.78$, $p < 0.01$)

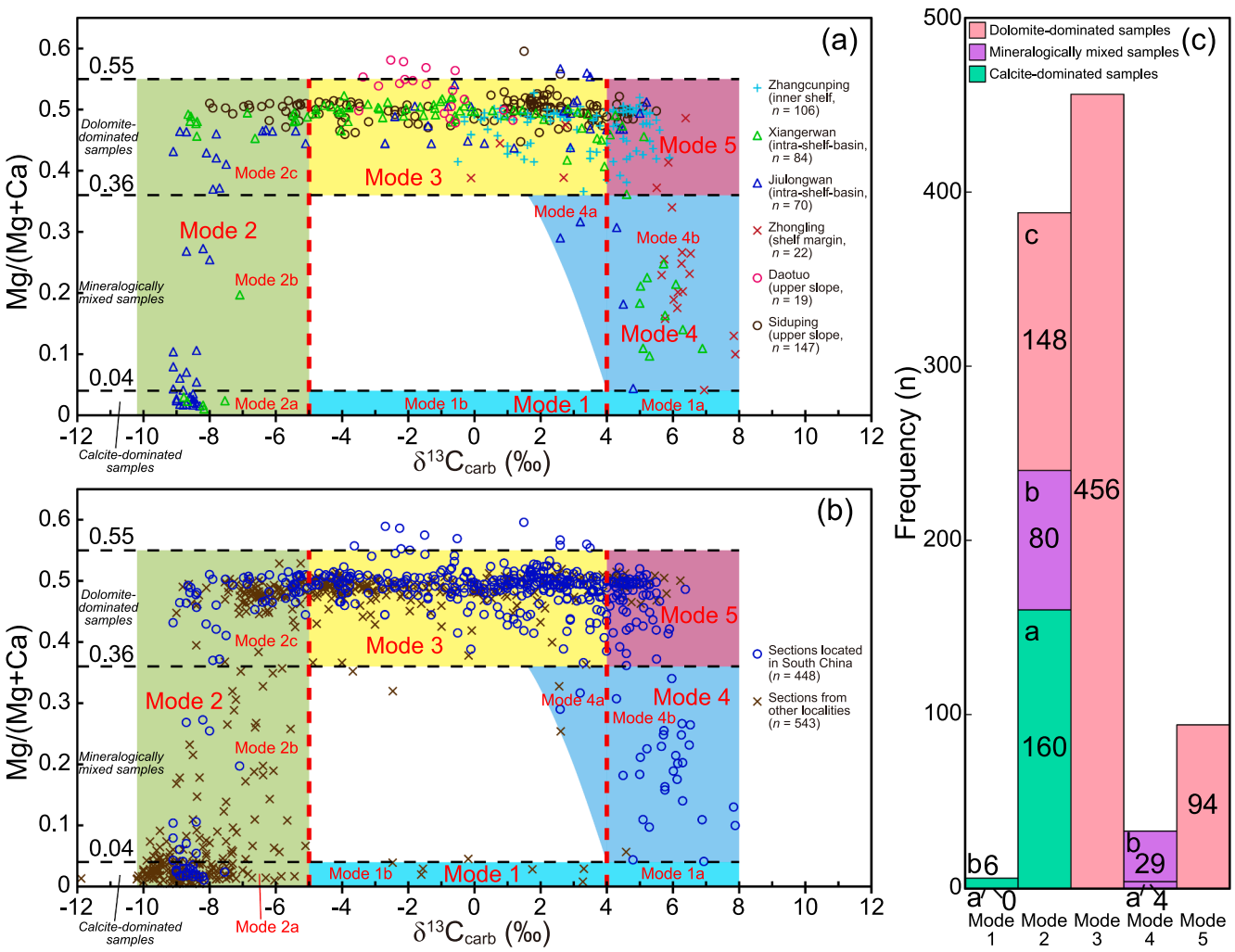

Fig. 4. Crossplots of $\delta^{13}C_{carb}$ versus Mg/(Mg + Ca) for all 17 study sections. (a) Data distribution of 6 study sections located in South China. (b) Data distribution of all 17 study sections globally. (c) Bar chart of sample quantity for each mode, the 14 samples out of modes are not included. Detailed data sources are listed in Table S1.

and Siduping ($n = 29$, $r = +0.63$, $p < 0.01$), but weaker relationships for Zhongling ($n = 10$, $r = +0.31$, $p \gg 0.10$), Huqf ($n = 43$, $r = -0.24$, $p > 0.10$) and Cerro Rajón ($n = 10$, $r = +0.25$, $p \gg 0.10$).

4.6. Ce/Ce*

Due to rare earth elements (REE) concentrations being much higher in detrital minerals than in carbonates, inputs of terrigenous materials (especially clays) can elevate the REE contents and mask seawater signatures in marine carbonates (Webb and Kamber, 2000). However, all REE data we collected were from samples treated with dilute acid, and the REE concentrations are from the carbonate fractions in this study (1-M HCl in Zhang et al., 2019, Cao et al., 2020; 2% HNO_3 in Chang et al., 2020), thus minimizing the influence of terrigenous detritus on measured REE values (Zhou et al., 2012; Zhang et al., 2019; Cao et al., 2020). Total REE concentrations are low, as expected for carbonates, i.e., <60 ppm at Zhangcunping and Bol'shoy Patom and <50 ppm at Jiulongwan and Siduping. REEs were normalized to PAAS (Post Archean Australian Shale; McLennan, 1989) in order to calculate Ce anomalies based on the equation: $Ce/Ce^* = Ce_n/([Pr]_n^2/[Nd]_n)$ (Lawrence et al., 2006; Ling et al., 2013), where n denotes normalization of concentrations against PAAS. The conventional equations for calculation of Ce anomalies, i.e., $Ce/Ce^* = 2 \times Ce_n/(La_n + Pr_n)$ and $Ce/Ce^* = 3 \times Ce_n/(2 \times La_n + Nd)$ (Bau and Dulski, 1996), were not adopted in the present study to prevent a spurious Ce-anomaly resulting from a positive La-anomaly (Wei et al., 2018). A crossplot of Ce/Ce* vs. $\delta^{13}C_{carb}$ (Fig. 8b) reveals a complicated relationship between these proxies: Ce/Ce* decreases from >1.0 to ~0.6 for $\delta^{13}C_{carb}$ from −9.8‰ to −5.0‰ (trend 1), recovers to near 1.0 for $\delta^{13}C_{carb}$ from −5.0‰ to +2.0‰ (trend 2), decreases again to ~0.6 for $\delta^{13}C_{carb}$ from +2.0‰ to +4.0‰ (trend 3), and then finally recovers to near 1.0 for $\delta^{13}C_{carb}$ > +4‰ (trend 4).

4.7. I/(Ca + Mg)

Nearly all samples have I/(Ca + Mg) values lower than 2.6 μmol/mol, a threshold commonly used to distinguish low-oxygen settings (<2.6 μmol/mol) from oxic settings (>2.6 μmol/mol) (Fig. 8c) (Lu et al., 2010, 2016; Glock et al., 2014; Hardisty et al., 2017; Wei et al., 2019b). Just three samples in the Huqf section have I/(Ca + Mg) > 2.6 μmol/mol, the highest (6.66 μmol/mol) being from a calcite-dominated sample. Overall, with $\delta^{13}C_{carb}$ values increasing, I/(Ca + Mg) values decrease except for a bulge (in red circle) associated with $\delta^{13}C_{carb}$ around +4‰.

5. Discussion

More than 70% of the samples we compiled in this study are dolomite-dominated samples (Fig. 4c; Table S1). The prevalence of

Fig. 5. XRD patterns of samples located in Mode 2–5 (a, b, c and d, respectively). Labels: C, calcite; D, dolomite; Q, quartz; F, fluorapatite.

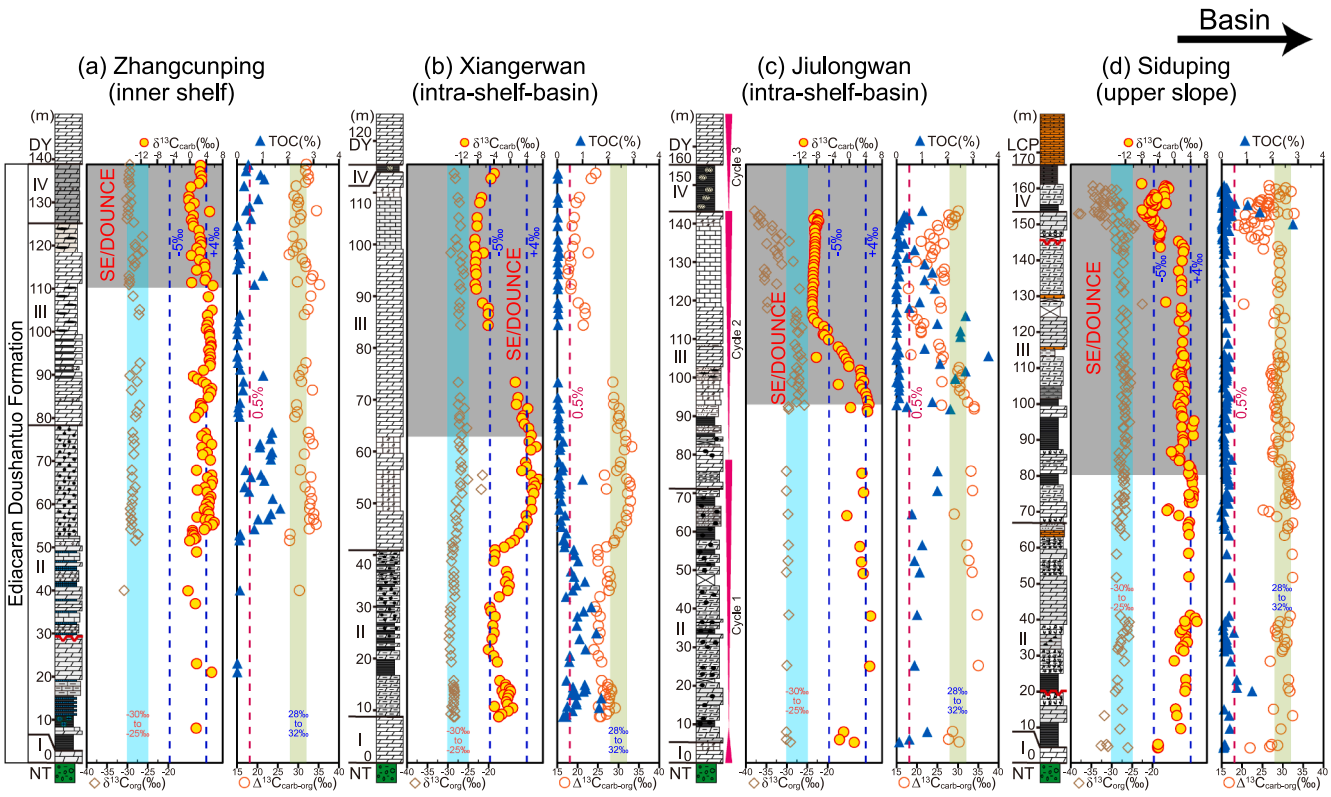

Fig. 6. $\delta^{13}C_{org}$, $\delta^{13}C_{carb}$, $\Delta^{13}C_{carb\text{-}org}$ and TOC profiles of the 4 study sections (a, Zhangcunping; b, Xiangerwan; c, Jiulongwan; d, Siduping) in South China with the direction from proximal to distal across the Yangtze Platform. Stratigraphic details and abbreviations are identical to those in Fig. 2. Detailed data sources are given in Table S1.

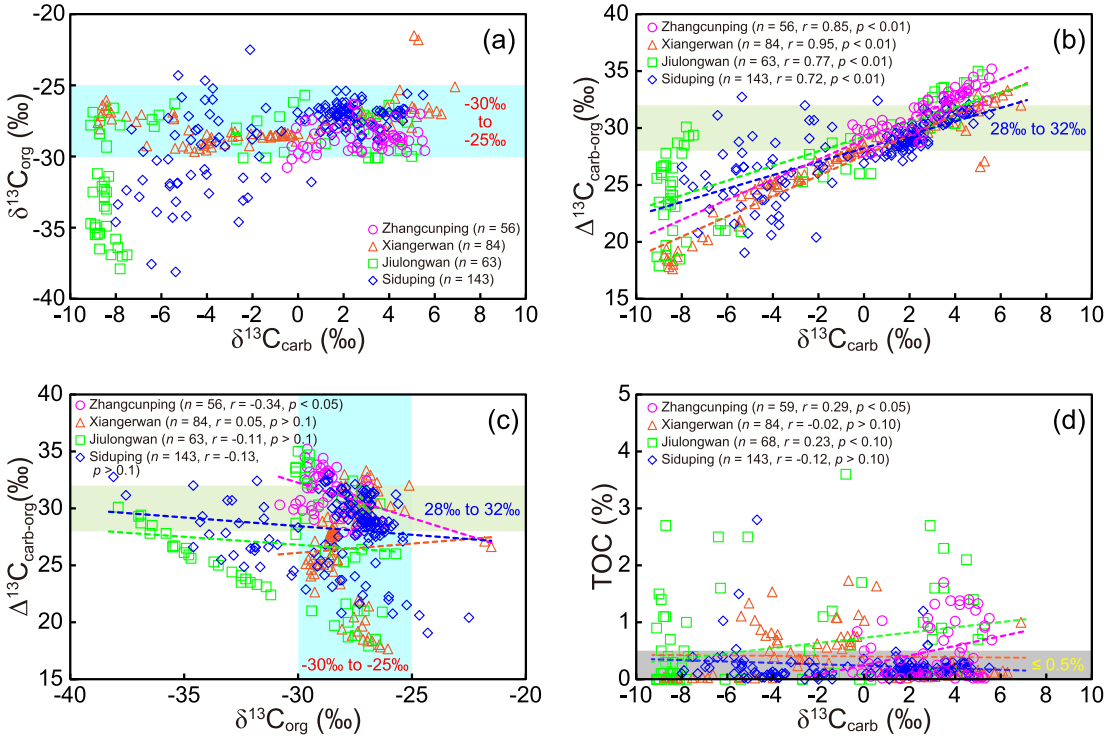

Fig. 7. Crossplots of $\delta^{13}C_{carb}$ versus $\delta^{13}C_{org}$ (a); $\delta^{13}C_{carb}$ versus $\Delta^{13}C_{carb\text{-}org}$ (b); $\delta^{13}C_{org}$ versus $\Delta^{13}C_{carb\text{-}org}$ (c) and $\delta^{13}C_{carb}$ versus TOC (d). Detailed data sources are listed in Table S1.

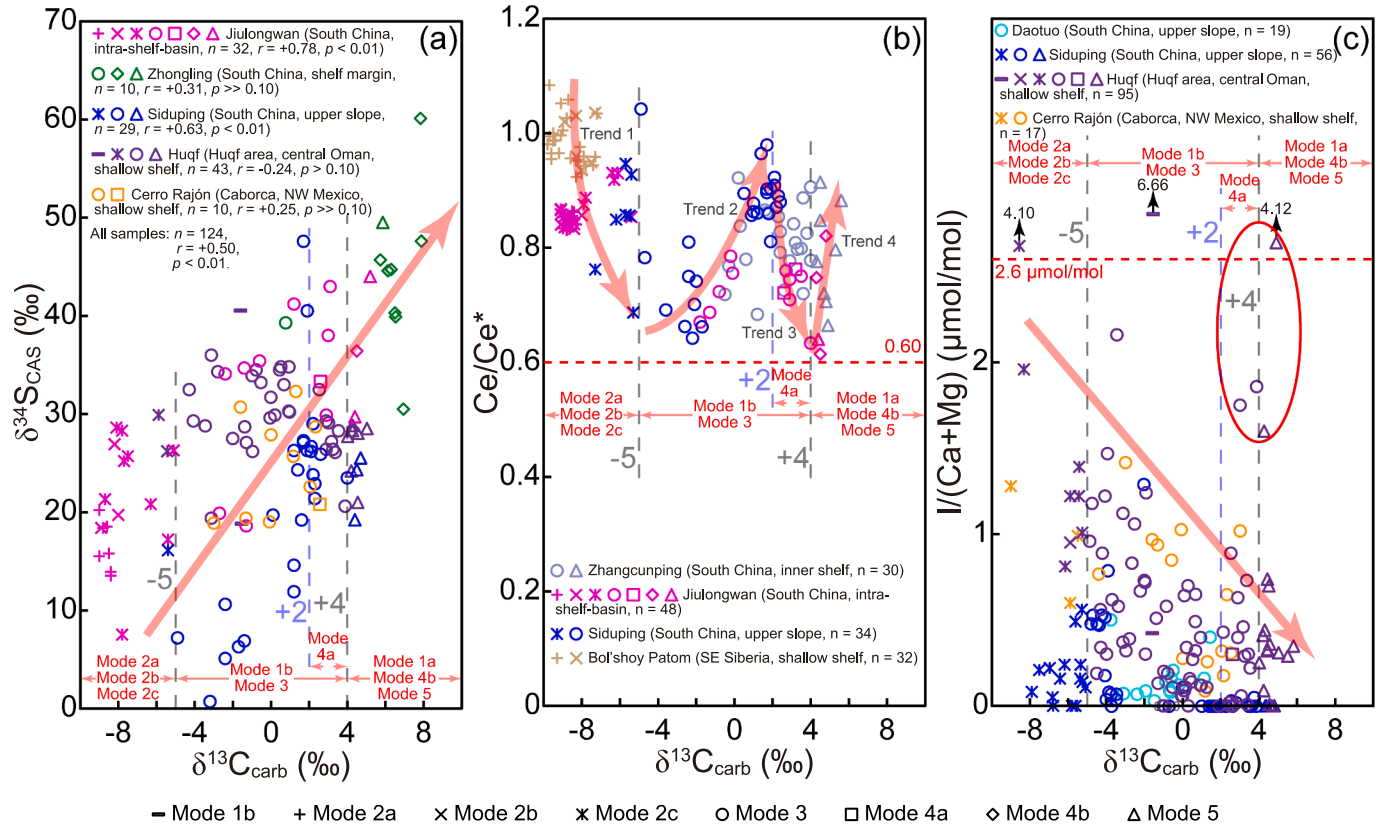

Fig. 8. Crossplots of $\delta^{13}C_{carb}$ versus $\delta^{34}S_{CAS}$ (a); $\delta^{13}C_{carb}$ versus Ce/Ce* (b) and $\delta^{13}C_{carb}$ versus I/(Ca + Mg) (c). The data from 14 samples out of modes are not shown. Detailed data sources are given in Table S1.

dolomite of late Ediacaran age underscores the reality of the "dolomite problem", i.e., that massive dolomites were precipitated in Precambrian oceans (Section 1). The study sections in South China, which form a proximal-to-distal (shelf-to-basin) transect across the Yangtze Platform, provide an expansive laboratory for us to explore the spatio-temporal distribution of calcite versus dolomite at a range of water depths and environmental conditions in the Ediacaran ocean (Fig. 2). In general, limestone and dolostone are intimately interbedded in the Ediacaran Doushantuo Formation (South China, Fig. 2a-d) and in many coeval successions in shallow settings globally (Fig. 3a, d-f, i-k), suggesting frequent shifts between calcite and dolomite precipitation in the Ediacaran ocean, whereas successions in deeper (e.g., upper slope) settings are dominated by dolomite (Fig. 2e-f). Some shallow-marine successions that lack dolomite-dominated (Fig. 3b, c) or calcite-dominated samples (Fig. 3g, h) may be insufficiently exposed to record mineralogic transitions. Moreover, the occurrence of calcite-dominated samples is usually accompanied by large negative $\delta^{13}C_{carb}$ excursions (<−5‰, Fig. 4b). Based on the "DOM catalyzation" and "large DOM reservoir" hypotheses (Section 1), we will mainly focus on the differences in seawater conditions favoring dolomite versus calcite precipitation, and explore their implications for massive dolomite formation in the Ediacaran ocean.

5.1. $\delta^{13}C_{carb}$ as a proxy for local DOM oxidation levels in Ediacaran ocean

The "large DOM reservoir hypothesis" is a viable explanation for the large negative $\delta^{13}C_{carb}$ excursions of the Ediacaran Period, in which large amounts of DOM were oxidized to generate ^{12}C-rich DIC and, thus, large negative shifts of $\delta^{13}C_{carb}$ (e.g., Rothman et al., 2003; Li et al., 2017). It has been inferred that the SE was caused by remineralization of a large DOM reservoir, possibly 100–1000× the mass of that in the modern ocean, based on geochemical modeling (Rothman et al., 2003). In the shallow ocean, photoautotrophs use DIC to produce organic matter, in which ^{12}C is preferentially incorporated, resulting in the residual DIC becoming ^{13}C-enriched (Farquhar et al., 1989). As organic matter sinks into the anoxic deep ocean and is broken down, it consumes available oxidants in the water column, intensifying anoxia and contributing to a DOM-rich deep ocean (Gao et al., 2018). Based on another geochemical modeling, it is estimated that the DOM reservoir in the Ediacaran ocean had a carbon mass about 20–30× larger than that of the modern DIC reservoir (Shields et al., 2019). Thus, the carbon isotopic composition of seawater DIC and in turn the $\delta^{13}C_{carb}$ was sensitive to the remineralization of the large DOM reservoir in the Ediacaran ocean (Swanson-Hysell et al., 2010; Wang et al., 2016b; Li et al., 2017; Gao et al., 2018; Xing et al., 2022).

In steady-state models of the carbon cycle, the relative magnitudes of the POM and inorganic carbonate burial fluxes modulate $\delta^{13}C_{carb}$ values (Kump, 1991), and the paired records of $\delta^{13}C_{carb}$ and $\delta^{13}C_{org}$ should vary in tandem when photosynthate is produced with a uniform fractionation relative to ambient DIC (Swanson-Hysell et al., 2010). This condition has prevailed during most of the last 800 million years, as shown by limited variation in sediment $\Delta^{13}C_{carb\text{-}org}$ between 28‰ and 32‰ (Hayes et al., 1999). In the present study units, however, $\delta^{13}C_{carb}$ exhibits large fluctuations whereas most $\delta^{13}C_{org}$ values (282 of 346 samples, or 81.5%) remain within the relatively narrow range of –30‰ to –25‰ (Figs. 6 and 7a), although small amount of samples (59 of 346 samples, or 17.1%) from the middle-late stage of the SE have $\delta^{13}C_{org}$ values <–30‰, which has generally been attributed to substantial contributions of organic matter produced by chemotrophic and/or methanotrophic organisms in deep anoxic watermasses (Jiang et al., 2012; Wang et al., 2016b; Li et al., 2017). This pattern resulted in large $\Delta^{13}C_{carb\text{-}org}$ fluctuations (from < +24‰ to > +33‰) within and among the study sections that are a function primarily of variation in $\delta^{13}C_{carb}$ (Fig. 7b) rather than in $\delta^{13}C_{org}$ (Fig. 7c). TOC > 0.5% is comparatively rare and corresponds to $\delta^{13}C_{carb}$

from <–5‰ to > +4‰, all four sections showing weak to no correlation of TOC with $\delta^{13}C_{carb}$ (Fig. 7d). These observations suggest a non-steady-state carbon cycle, in which the POM burial flux was small and well-buffered by the large DOM reservoir in the Ediacaran ocean, thus resulting in POM having negligible influence on the $\delta^{13}C_{carb}$ record.

In summary, if the marine DOM reservoir in the Ediacaran ocean was large, then the magnitude of local $\delta^{13}C_{carb}$ fluctuations can potentially be used as a proxy to estimate changes in local marine DOM oxidation levels, with positive excursions representing minimal DOM remineralization due to limited DOM or oxidant availability, and negative excursions representing strong DOM remineralization due to an adequate supply of both DOM and oxidants.

5.2. Local DOM concentrations and its oxidation levels inferred by Modes 1–5

In the "DOM catalyzation hypothesis", despite variation in DOM reactivity, increases in DOM promote incorporation of Mg^{2+} into the lattice of carbonates, probably due to enhancement of functional groups (Zhang et al., 2012b; Liu et al., 2020). The local DOM concentrations and DOM oxidation levels in the Ediacaran ocean can be inferred from Fig. 4b, in which higher Mg/(Mg + Ca) was associated with greater local concentration of DOM and lower $\delta^{13}C_{carb}$ was associated with greater local oxidation of DOM. The samples in Mode 5, which are dolomite-dominated and have high $\delta^{13}C_{carb}$, may have been precipitated mainly from a watermass with high DOM concentrations that favored protodolomite formation but with little or no DOM oxidation. The samples in Mode 2, which include calcite-dominated (Mode 2a), mixed (Mode 2b), and dolomite-dominated (Mode 2c) samples having extremely low $\delta^{13}C_{carb}$ (<−5‰), may have formed from a watermass characterized by substantial DOM oxidation and variable DOM concentrations that episodically overcame the threshold for protodolomite precipitation. Mode 3, which is transitional between Modes 2 and 5, was subject to intermediate levels of DOM oxidation but with nonetheless sufficient DOM concentrations for protodolomite formation. Mode 1, which is characterized by higher $\delta^{13}C_{carb}$ than Mode 2, consists of calcite-dominated samples that may have precipitated from a watermass where DOM was present in extremely low concentrations, thus precluding generation of ^{13}C-depleted DIC as well as protodolomite formation. Mode 4, which is located between Modes 1, 3, and 5, consists of samples of mixed mineralogy and likely to formed under conditions intermediate between those of Modes 1, 3, and 5.

5.3. A DOM regulation model for calcite versus dolomite precipitation in the Ediacaran ocean

As indicated in Section 1, the DOM catalyzation hypothesis used in this study represents a primary dolomite formation mechanism. However, many secondary dolomite formation models involving various dolomitizations can also be potentially used to account for the massive formation of Precambrian dolomite. Dolomitization can occur in near-surface, burial, or hydrothermal settings (see review by Cai et al., 2021). Near-surface dolomitization is a feature of the sabkha and seepage-reflux models, which invoke hydrologically restricted environments with high evaporation rates and hypersaline watermasses (Machel, 2004). Although shelf sections in South China are thought to represent relatively restricted lagoonal environments (Jiang et al., 2011), these models cannot explain that the upper-slope Daotuo and Siduping sections accumulated only dolomite-dominated samples (Fig. 2e, f). The burial and hydrothermal dolomitization models invoke alteration of primary limestones by Mg^{2+}-rich fluids at high temperatures (usually >60 °C; Gregg et al., 2015), causing significant increases of crystal size and/or Mn/Sr ratios (Kaufman and Knoll, 1995; Warren, 2000; Du et al., 2018; Garaguly et al., 2018; Ngia et al., 2019). Recently, the diffusion-advection-reaction model was proposed as a mechanism for large-scale dolomitization in early diagenetic settings (Huang et al., 2015), but it focuses on the source of Mg^{2+} and ignores the importance of overcoming the energy barrier of Mg^{2+} hydration. Our samples were all screened for potential secondary diagenetic alteration, with only those having microcrystalline structure and Mn/Sr ratios of <10 being included in the final dataset (see Section 2). In addition, clumped-isotope (Δ_{47}) paleotemperatures for the Zhangcunping section document dolostone precipitation at temperatures of <60 °C (Chang et al., 2020), which does not support the burial or hydrothermal models for dolomite formation in this study. In summary, these secondary dolomite formation models cannot fully account for the spatiotemporal pattern of calcite versus dolomite precipitation in the Ediacaran ocean observed in this study. Next, based on inferred DOM concentrations and its oxidation levels by Modes 1–5 (as described in Section 5.2), we explore the utility of the DOM catalyzation hypothesis and its possible relationship to local DOM regulation within the framework of known Ediacaran ocean chemistry.

Although details of its redox structure remain uncertain, the Ediacaran ocean is inferred to have been highly redox-stratified, at least in shelf areas, where it consisted of an oxic surface layer, a metastable sulfidic mid-depth layer ("euxinic wedge"), and an anoxic (ferruginous) deep layer (c.f., Li et al., 2010, and reviewed by Li et al., 2020a). This redox structure was favored by low atmospheric O_2 levels, overall low oceanic sulfate and other oxidant concentrations, and low vertical mixing rates on shelves (Li et al., 2018, 2020a). This scenario may have caused localized oxidation of DOM in near-surface more-oxic marine environments, producing a local decrease in DOM concentrations and lower DIC-$\delta^{13}C$ values, whereas the distal deep watermass remained anoxic with high DOM levels. Such a lateral environmental gradient has been used to account for the large spatial heterogeneity of Ediacaran carbon isotope records (Li et al., 2017).

Based on the discussion above and in Section 5.2, we hypothesize that dolomite formation in the Ediacaran ocean was DOM-regulated (Fig. 9). In this "DOM regulation model", the redox-stratified Ediacaran ocean exhibits a DOM gradient with increasing concentrations toward distal, deeper anoxic facies due to decreasing oxidant (e.g., O_2 and sulfate) availability. The boundary between the oxic surface layer and the anoxic deep layer is a DOM anaerobic oxidation zone, in which DOM is partly anaerobic oxidized by sulfate and other oxidants (e.g., Fe^{3+}) and converted to DIC, resulting in a higher alkalinity and conducive to carbonate formation. This anaerobic oxidation zone becomes narrower and shallower distally (i.e., oceanward), which is also due to decreasing oxidant availability. Greater oxidant availability in nearshore areas is caused by weathering inputs of sulfate and other oxidants (e.g., Fe^{3+}), and by greater photosynthetic O_2 production fueled by riverine nutrient fluxes (Reinhard et al., 2016; Li et al., 2017). Considering that carbonate deposition was predominantly a chemical process prior to the appearance of biocalcification in the Cambrian (Ridgwell and Zeebe, 2005; Kazmierczak et al., 2013) and thus different from the metazoan-mediated carbonate production of the modern ocean (Keil and Annual, 2017), it may have occurred through one of three reaction pathways: (1) microbially mediated photosynthetic consumption of CO_2 within the ocean-surface layer, increasing watermass alkalinity ("photosynthesis pathway"); (2) microbially mediated precipitation during anaerobic decomposition of organic matter, increasing carbonate alkalinity in certain areas (i.e., the DOM anaerobic oxidation zone in this study) ("OM decomposition pathway"); and (3) direct abiotic precipitation from seawater, which would require unusually high carbonate mineral saturation levels ("saturation pathway") (Shields, 2005).

In our model (Fig. 9), carbonate precipitation through the photosynthetic pathway occurred in the upper water column (i.e., the "carbonate formation zone), diminishing with depth until reaching zero at the "carbonate precipitation threshold", and calcite was precipitated in the upper oxic surface layer with little or no DOM, whereas the dolomite was precipitated in the anoxic deep layer with high DOM. There was also localized carbonate precipitation in the DOM anaerobic oxidation zone

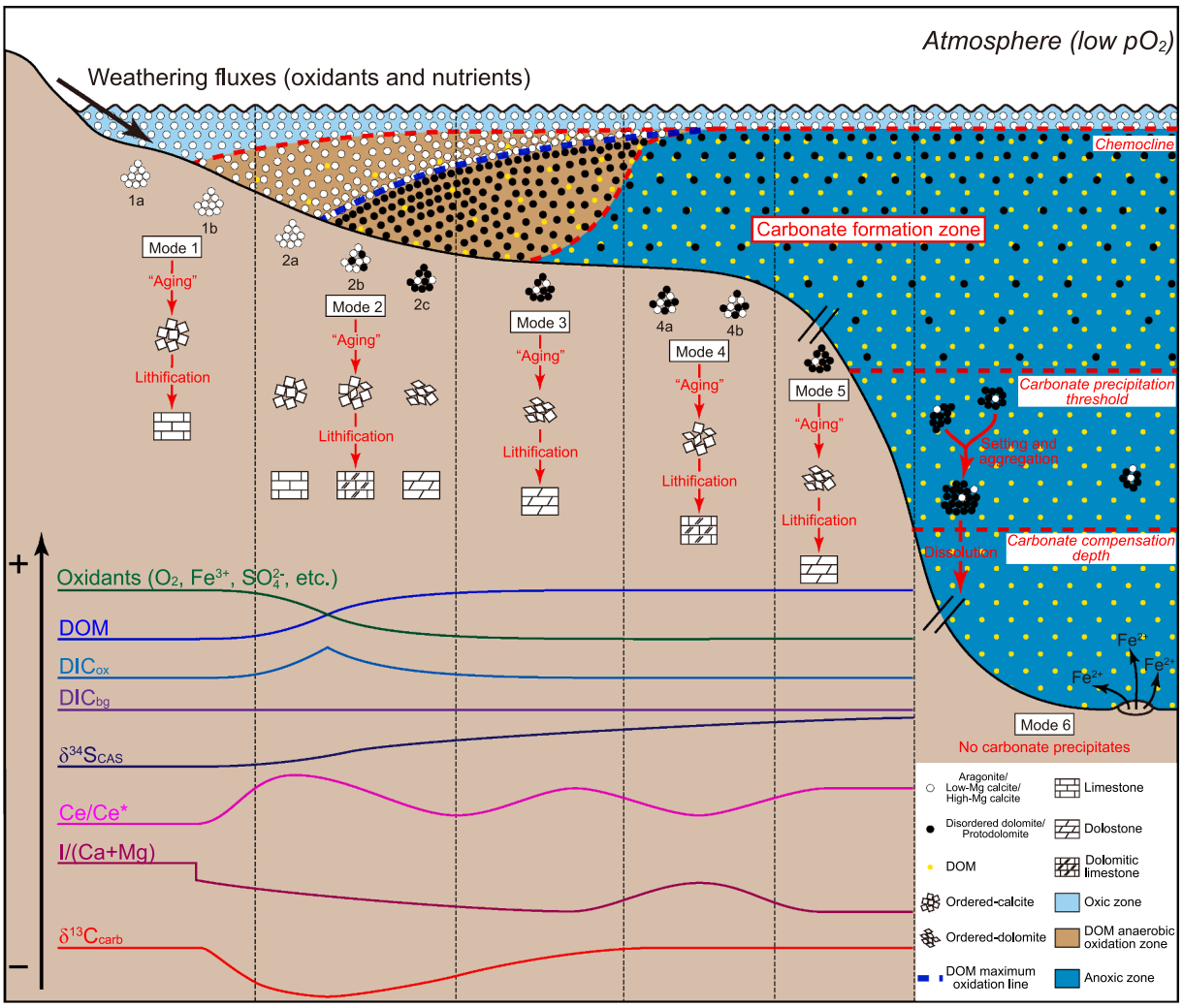

Fig. 9. Schematic representation of the DOM regulation model involving heterogeneous carbonate mineral formation in this study. Modes 1–5 correspond to different Mg/(Mg + Ca) and $\delta^{13}C_{carb}$ relationships (see Fig. 4b), and Mode 6 represents the lack of carbonate production below the carbonate compensation depth (CCD). Abbreviations: DIC = dissolved inorganic carbon, with DIC_{ox} derived from local oxidation of subsurface dissolved organic matter (DOM), and DIC_{bg} representing the global marine DIC background. The trend lines of oxidants (O_2, Fe^{3+}, SO_4^{2-}, etc.), DOM, DIC_{ox} and DIC_{bg} refer to proposed seawater chemistry, while the trend lines of $\delta^{34}S_{CAS}$, Ce/Ce*, I/(Ca + Mg) and $\delta^{13}C_{carb}$ refer to proposed geological records preserved in sediments. See text for more details.

driven by the OM decomposition pathway. In this zone, the mineralogy of carbonate precipitates was influenced by local DOM concentrations, with higher DOM catalyzing greater Mg uptake into the carbonate crystal lattice, favoring dolomite formation. Sinking carbonate minerals underwent dissolution owing to falling saturation levels with depth, with complete loss of carbonate at the carbonate compensation depth (CCD) (Fig. 9). The $\delta^{13}C_{carb}$ of these precipitates was determined by the flux of ^{13}C-depleted DIC from local DOM oxidation (DIC_{ox}) relative to the more ^{13}C-rich background DIC (DIC_{bg}) that was in equilibrium with atmospheric CO_2. Within this model framework, five modes with different Mg/(Mg + Ca) and $\delta^{13}C_{carb}$ relationships (i.e., Modes 1–5 in Fig. 4b) can be linked to an environmental gradient extending from nearshore areas to the distal ocean (Fig. 9).

Mode 1, located in the nearshore zone, is characterized by low DOM levels. Based on the presence or absence of DOM anaerobic oxidation, it can be subdivided into Modes 1a and 1b. In Mode 1a, the whole water column is oxic with high $\delta^{13}C$, and in Mode 1b surface waters are oxic with high $\delta^{13}C$ (ranging from +4‰ to +8‰), but the deeper waters are suboxic with variable $\delta^{13}C$ (–5‰ to +4‰) due to limited amounts of DOM anaerobic oxidation. The areal extent of Mode 1 was likely limited because of low atmospheric O_2 levels in the Ediacaran (i.e., only a few percent of present atmospheric level, or PAL; see reviews by Sperling et al., 2015; Lyons et al., 2021). Furthermore, the record of Mode 1 may be limited owing to erosion of nearshore deposits during marine regressions, as recorded in the Doushantuo Formation (McFadden et al., 2008; Jiang et al., 2011), which may explain the relative paucity of Mode 1 samples (Fig. 4b, c).

Mode 2, located in inner-shelf areas adjacent to Mode 1, is characterized by large-scale DOM anaerobic oxidation and increasing DOM concentrations in the suboxic lower water column. In this mode, limited amounts of isotopically heavy calcite precipitate from the oxic surface layer, while large amounts of isotopically light calcite and dolomite form in the suboxic lower water column due to large-scale DOM anaerobic oxidation. The more proximal part of this mode is dominated by calcite precipitation (Mode 2a), shifting to mixed (Mode 2b) and dolomite-dominated sediments (Mode 2c) in the offshore direction (Fig. 4b and 5a). The DOM anaerobic oxidation zone is likely to have expanded in volume when weathering fluxes increased, as during the SE (Li et al., 2017), enhancing Mode 2 sedimentation. This process may explain Mode 2 samples (Fig. 4b) that are associated with large negative $\delta^{13}C_{carb}$ excursions (Figs. 2 and 3).

Mode 3, located on the middle shelf adjacent to Mode 2, is characterized by high deep water DOM levels but decreasing anaerobic oxidation of DOM. In this mode, dolomite is the dominant carbonate

mineral formed due to high DOM concentrations in the thick suboxic-anoxic lower water column, although some calcite is produced in the upper water column where little DOM is present. However, due to decreasing oxidant availability distally in the Ediacaran ocean, the rate of DOM anaerobic oxidation declines, allowing $\delta^{13}C_{carb}$ to gradually increase from <−5‰ for Mode 2 to ~+4‰ for Mode 4 (Fig. 4b), even though all of these samples are dolomite-dominated (Fig. 5b).

Mode 4, located in outer-shelf areas adjacent to Mode 3, is at the distal end of the DOM anaerobic oxidation zone. In this mode, the production of isotopically light carbonates by DOM anaerobic oxidation ranges from minor (Mode 4a) to zero (Mode 4b). Production of isotopically heavy calcite in the thin oxic surface layer was comparable in amount to that of isotopically heavy dolomite in the thick anoxic lower water column because carbonate precipitation rates were lower in the latter given limited photosynthetic utilization of CO_2 and low alkalinity (Shields, 2005). This setting accumulated mineralogically mixed samples with a range of $\delta^{13}C_{carb}$ values (~+2‰ to +4‰ for Mode 4a, and >+4‰ Mode 4b; Fig. 4b and 5c).

Mode 5, located in outer-shelf to slope areas adjacent to Mode 4, is also characterized by the lack of DOM anaerobic oxidation, as in Mode 4. However, the anoxic lower water column in Mode 5 is broader in vertical dimension than that in Mode 4, which would make more isotopically heavy dolomite produced in spite of lower microbially mediated removal of CO_2 and lower alkalinity with depth (Shields, 2005), whereas the isotopically heavy calcite produced in the thin oxic surface layer in this mode is the same as in Mode 4. Consequently, the mixture of these carbonate minerals is dolomite-dominated in Mode 5 with a heavy $\delta^{13}C_{carb}$ signature (>+4‰; Fig. 4b and 5d).

Mode 6, located in slope to basinal areas adjacent to Mode 5, is characterized by the lack of DOM anaerobic oxidation and water depths that exceed the carbonate compensation depth. As a consequence, any carbonate formed in the overlying water column was dissolved below the CCD, resulting in no carbonate preservation in the sediment (i.e., siliciclastic facies; Fig. 4b). Owing to its lack of carbonate, no samples of Mode 6 were collected in this study.

Our new DOM regulation model seems to explain well the unusual relationship of Mg/(Mg + Ca) and $\delta^{13}C_{carb}$ values in the study units (Fig. 4b) as well as their spatiotemporal distributions (Figs. 2 and 3) and inferred redox structure in Ediacaran ocean (Li et al., 2010, 2020a). We note that the six modes outlined in our model should be considered as spatiotemporally dynamic within a given region because many additional factors might affect key parts of our model. For example, sea-level fluctuations related to marine transgression and regression can affect local water depths (e.g., McFadden et al., 2008 for Jiulongwan, and Zhu et al., 2007 for Zhongling), changing the position of a given section relative to the DOM anaerobic oxidation zone; enhanced continental weathering may expand the volume of the DOM anaerobic oxidation zone and increase rates of DOM anaerobic oxidation, thus affecting calcite and dolomite fluxes to the sediment as well as $\delta^{13}C_{carb}$ values. These dynamics may account for samples from a single section occupying several modes in Fig. 4a-b (e.g., Jiulongwan and Xiangerwan in South China, and Huqf in Oman).

5.4. Redox evidence for the DOM regulation model

Whilst questions remain as to the mechanism of sulfate (SO_4^{2-}), REEs and iodate (IO_3^-) incorporation into carbonate minerals, carbonates have been shown to faithfully record the isotopic composition of SO_4^{2-}

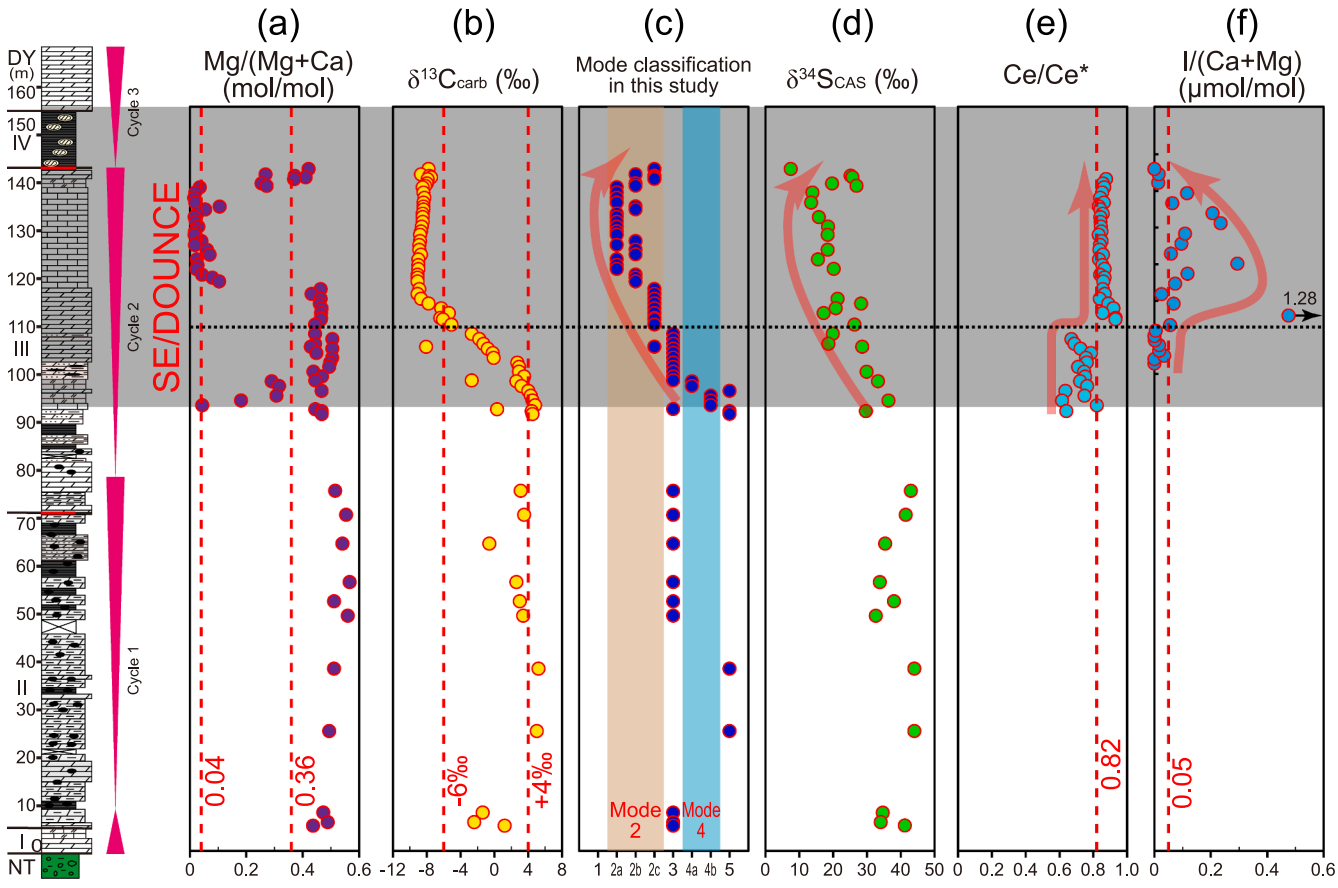

Fig. 10. Mg/(Mg + Ca) (a), $\delta^{13}C_{carb}$ (b), mode classification (c) [for better contrast, sub-modes (Modes 2a, 2b and 2c, Modes 4a and 4b are also shown; cf. Fig. 4b)] in this study and multiple redox proxies [$\delta^{34}S_{CAS}$ (d), Ce/Ce* (e) and I/(Ca + Mg) (f)] profiles of Jiulonghwan section. Stratigraphic details and abbreviations are identical to those in Fig. 2. The data of I/(Mg + Ca) is from Wei et al. (2019b) and other detailed data sources are given in Table S1.

(by CAS, with no apparent fractionation), and the concentrations of REEs and IO_3^- (subject to partitioning coefficients) of the ambient watermass, providing information about ancient marine redox environments (Burdett et al., 1989; Zhong and Mucci, 1995; Kampschulte et al., 2001; Kampschulte and Strauss, 2004; Lu et al., 2010; Rennie and Turchyn, 2014; Tostevin et al., 2016a, 2016b; Zhang and Shields, 2022; Li et al., 2022). Here, we use available data for selected redox proxies [i.e., $\delta^{34}S_{CAS}$, Ce anomaly, and I/(Ca + Mg)] (Fig. 10) to test the expected chemical conditions of each carbonate precipitate mode shown in Fig. 9, which strongly support our DOM regulation model.

(1) $\delta^{34}S_{CAS}$ versus $\delta^{13}C_{carb}$. Generation of sulfide occurs principally through microbial sulfate reduction (MSR), which generally represents the largest portion of anaerobic organic carbon oxidation in marine sediments (Kasten and Jørgensen, 2000). Preferential reduction of ^{32}S-bearing SO_4^{2-} to H_2S and its subsequent burial as pyrite (given sufficient iron availability) causes the residual pool of aqueous sulfate to become enriched in ^{34}S, a signal that can be preserved by CAS. Given a limited oceanic sulfate reservoir, consumption of SO_4^{2-} leads to higher $\delta^{34}S$ values in the residual SO_4^{2-} until its complete depletion (Berner, 1984; Canfield and Thamdrup, 1994; Canfield, 2001; Loyd et al., 2012a). In the study units, $\delta^{34}S_{CAS}$ is highly variable (from +0.7‰ to +60.1‰; Fig. 8a), reflecting sustained low sulfate concentrations in the Ediacaran ocean (cf. Kah et al., 2004; Hurtgen et al., 2005; Canfield et al., 2010; Loyd et al., 2012b; Algeo et al., 2015). $\delta^{13}C_{carb}$ and $\delta^{34}S_{CAS}$ exhibit a moderate positive correlation for the full sample set ($n = 124$, $r = +0.50$, $p < 0.01$) but non-significant relationships for individual sections: Zhongling ($n = 10$, $r = +0.31$, $p \gg 0.10$), Huqf ($n = 43$, $r = -0.24$, $p > 0.10$), and Cerro Rajón ($n = 10$, $r = +0.25$, $p \gg 0.10$) (Fig. 8a), suggesting strong spatial (rather than temporal) heterogeneity of DOM anaerobic oxidation and MSR in the Ediacaran ocean, consistent with previous studies (Li et al., 2010; 2017; Shi et al., 2018) and our DOM regulation model proposed in Section 5.3. The lack of significant relationships for individual sections may be due to their relatively narrow $\delta^{13}C_{carb}$ ranges (+0.77‰ to +7.88‰ in Zhongling, –5.89‰ to +5.03‰ in Huqf, –3.00‰ to +2.56‰ in Cerro Rajón) and/or limited sample numbers. The negative excursions in $\delta^{34}S_{CAS}$ and $\delta^{13}C_{carb}$ during the SE were synchronous (Fig. 8a), which is interpreted to reflect an increase in the marine sulfate concentrations of shallow-marine watermasses (Li et al., 2017). Considering that a large proximal-to-distal SO_4^{2-} concentration gradient likely existed in the Ediacaran ocean as proposed by Shi et al. (2018) and Li et al. (2020a), the samples with low $\delta^{13}C_{carb}$ and low $\delta^{34}S_{CAS}$ (Modes 2 and 3) are inferred to have formed mainly in proximal shallow waters with relatively high SO_4^{2-} concentrations, whereas the samples with high $\delta^{13}C_{carb}$ (Modes 4 and 5) accumulated mainly in distal deeper waters with low SO_4^{2-} concentrations, these are all in line with our model (Fig. 9).

(2) Ce/Ce* versus $\delta^{13}C_{carb}$. In oxygenated seawater, soluble Ce(III) is readily oxidized to insoluble Ce(IV), which desorbs much less efficiently from particulate matter, leading to a considerable depletion of seawater Ce relative to its REE neighbors (i.e., a negative Ce anomaly, Ce/Ce* < 1) (Debaar et al., 1985; Michard and Albarede, 1986; Sholkovitz et al., 1994; Bau and Koschinsky, 2009). In the study, Ce/Ce* data ($n = 144$) are from Modes 2–5, with no data available from Mode 1. All available Ce/Ce* data in our study are more than 0.60 (Fig. 8b), consistent with that carbonate precipitation in Modes 2–5 are mainly from a dominantly suboxic to anoxic watermass proposed in our model (Fig. 9), similar to the subsurface waters of the modern Black Sea (Slack et al., 2007; Ling et al., 2013). In general, the increase of $\delta^{13}C_{carb}$ represents a distal deeper water with decreasing SO_4^{2-} concentrations as shown in $\delta^{34}S_{CAS}$ proxy above, the Ce/Ce* values should have increase simultaneously. However, only samples in Trend 2 and Trend 4 in Fig. 8b recorded the expected increase in Ce/Ce* values, whereas the samples in Trend 1 and Trend 3 recorded a decrease in Ce/Ce* values. Considering that the reductive dissolution of Fe/Mn-(oxyhydr)oxides and/or remineralization of organic matter can also lead to higher Ce/Ce* under low-oxygen marine conditions (Debaar et al., 1988; German et al., 1991; Bau et al., 1997), Trend 1, which represents a decrease of Ce/Ce* values from Mode 2a (mean 0.94, $n = 40$) to Mode 2b (mean 0.90, $n = 15$), and to Mode 2c (mean 0.86; $n = 16$) in Fig. 9, is consistent with a reduced Ce contribution from reductive dissolution of Fe/Mn-(oxyhydr)oxides and/or remineralization of DOM controlled by the availability of terrigenously sourced oxidants (O_2, Fe^{3+}, SO_4^{2-}, etc.) because Mode 2a is closest to terrigenous than Mode 2b and Mode 2c. Trend 3 involves dolomite-dominated samples in Mode 3 (Ce/Ce* mean 0.81, $n = 59$) and mixed samples in Mode 4a (Ce/Ce* mean 0.74, $n = 2$) with $\delta^{13}C_{carb}$ between +2‰ to +4‰ (Fig. 4b). The decreasing Ce/Ce* values in Trend 3 may represent a local increase in the ratio of calcite (with low Ce/Ce* precipitated in the upper oxic surface layer) versus dolomite (with high Ce/Ce* precipitated in the anoxic deep layer) in total carbonate precipitation. When this ratio returns to decrease, the Ce/Ce* values switch to increase as shown in Trend 4 which involves samples in Mode 4b (Ce/Ce* mean 0.73, $n = 3$) and Mode 5 (Ce/Ce* mean 0.77, $n = 9$). Trend 2 involves mainly samples from Mode 3. The increase in Ce/Ce* values in Trend 2 may represent a normal water-column redox gradient when the Ce contribution from reductive dissolution of Fe/Mn-(oxyhydr)oxides and/or remineralization of DOM decreased to insignificance. Taken together, the specific trends of Ce/Ce* values observed in this study (Fig. 8b) provide signature evidence for our proposed DOM regulation model (Fig. 9).

(3) I/(Ca + Mg) versus $\delta^{13}C_{carb}$. Dissolved iodine in seawater consists of the oxidized form iodate (IO_3^-) and the reduced form iodide (I^-) (Emerson et al., 1979; Chance et al., 2014). IO_3^- exists exclusively in oxic waters and is quantitatively reduced to I^- in weakly oxic waters (i.e., dysoxic; Algeo and Li, 2020) prior to the onset of iron and sulfate reduction (Wong and Brewer, 1977; Rue et al., 1997; Hardisty et al., 2017). The decomposition of organic matter in an oxic water column releases IO_3^- back to seawater (Van Cappellen and Ingall, 1994; Lu et al., 2010, 2016). Given that IO_3^- is the sole iodine species that co-precipitates with carbonate minerals, carbonates precipitated from oxic waters tend to have high I/(Ca + Mg) ratios (>2.6 μmol/mol) (Lu et al., 2010, 2016; Hardisty et al., 2017; Wei et al., 2019b). Diagenetic alteration may lower but does not increase the I/(Ca + Mg) ratios of carbonate rocks (Lu et al., 2010; Hardisty et al., 2017; Wei et al., 2019b). In the study units, nearly all available I/(Ca + Mg) data are lower than 2.6 μmol/mol (Fig. 8c), indicating that the local watermass from which carbonates precipitated was mainly suboxic to anoxic, in agreement with the Ce/Ce* data. With increasing $\delta^{13}C_{carb}$, I/(Ca + Mg) tends to decrease generally from Mode 2 to Mode 3 and then Mode 5 samples (Fig. 8c), indicating that the carbonates with higher $\delta^{13}C_{carb}$ (e.g., Mode 5) formed under more reducing conditions relative to the carbonates with lower $\delta^{13}C_{carb}$ (e.g., Modes 2–3), consistent with our DOM regulation model proposed in Section 5.3. However, there is a bulge of I/(Ca + Mg) values associated with $\delta^{13}C_{carb}$ near +4‰ (2 data from Mode 3 and 2 data from Mode 5; Fig. 8c). This anomaly is similar to what observed in Ce/Ce* around +4‰ of $\delta^{13}C_{carb}$ (Fig. 8b), can be similarly explained by a local change around Mode 4 in the ratio of calcite [with high I/(Ca + Mg) precipitated in the upper oxic surface layer] and dolomite [with low I/(Ca + Mg) precipitated in the anoxic deep layer] to total carbonate precipitation (see Fig. 9). There should be the highest I/(Ca + Mg) values around the boundary between Mode 4a and Mode 4b due to more calcite precipitated. However, just one sample [I/(Ca + Mg) = 0.3] was collected in this mode, leading to a missing of these highest values although a bulge of I/(Ca + Mg) values is defined by 4 samples from adjacent Mode 3 and Mode 5. Although the samples located in Mode 1 are rare in our compiled dataset, it should be noted that a Mode 1 sample has the highest I/(Ca + Mg) value (6.66), further supporting the idea that Mode 1 represents relatively more oxic conditions. Taken together, the relationships of I/(Ca + Mg) versus $\delta^{13}C_{carb}$ also support our model well (Fig. 9).

As an example, the stratigraphic coupling of mode classification, and

coexisting Mg/(Mg + Ca), $\delta^{13}C_{carb}$, and redox [$\delta^{34}S_{CAS}$, Ce/Ce* and I/(Ca + Mg)] records observed in the Jiulongwan section (South China) also provide additional evidence for our new model (Fig. 10). Our mode classification (Fig. 10c) shows the same pattern as $\delta^{34}S_{CAS}$ (Fig. 10d), supporting the inference that sulfate/oxidants availability controlled DOM oxidation because lower $\delta^{34}S_{CAS}$ (e.g., during the SE) was associated with higher sulfate availability (see mechanism explanation above), which caused more DOM anaerobic oxidation, and lower DOM levels, eventually resulting in lower $\delta^{13}C_{carb}$ (Fig. 10b) and Mg/(Mg + Ca) (Fig. 10a), and a shallower-water mode (Fig. 10c). Specifically, the increases of Ce/Ce* (from <0.82 to >0.82; Fig. 10e) and I/(Ca + Mg) (from 0.01 to 0.17 in average; Fig. 10f) during the SE indicate a shift from anoxic to suboxic conditions along with an increase in DOM oxidation in the Jiulongwan section, which accords with our mode classification from Mode 5 to Mode 2 (Fig. 10c).

5.5. Key implications for the "dolomite problem"

Our DOM regulation model for calcite versus dolomite precipitation in the Ediacaran ocean has important implications for the "dolomite problem". The key boundary conditions for our model are (1) a stratified redox structure in the ocean, (2) a large DOM reservoir in the anoxic deep ocean, and (3) oxidant availability in shallow shelf areas. These conditions promoted development of a metastable DOM anaerobic oxidation zone between the oxic surface layer and the anoxic deep watermass, which operated most vigorously in shelf areas (see Section 5.3). Recent research indicates that early oceans were mostly anoxic, and that the deep oceans were not fully oxygenated until the early Cambrian at the earliest (Chen et al., 2015) and possibly as late as the Devonian (Dahl et al., 2010; Stolper and Keller, 2018; Stolper and Bucholz, 2019; see reviews by Lyons et al., 2014, 2021 and Li et al., 2020a). Accordingly, Precambrian and early Cambrian oceans were most likely redox stratified with an oxic surface layer and an anoxic deep watermass (cf. reviews by Poulton and Canfield, 2011; Lyons et al., 2014, 2021; Li et al., 2020a). So-called "deep-ocean oxygenation events" during the Ediacaran and early Cambrian were most likely temporary shelf oxygenation events boosted by transiently elevated oxidant and nutrient fluxes into shelf areas due to enhanced continental weathering (see review by Li et al., 2018). A large DOM reservoir is envisioned mainly for the Neoproterozoic ocean based on highly negative $\delta^{13}C_{carb}$ excursions such as the SE, during which $\delta^{13}C_{carb}$ fell far below the mantle value of ~−5‰ and exhibited decoupling from coeval $\delta^{13}C_{org}$ records (cf. Grotzinger et al., 2011; Li et al., 2017). However, given that early oceans were mostly anoxic, it is reasonable to infer that the DOM reservoir of the anoxic deep watermass was much larger than that of today's oxic deep ocean. Since the key boundary conditions of our DOM regulation model for dolomite formation existed widely in early oceans, this model represents a novel mechanism for deep-time massive dolomite precipitation, providing an alternative view on the origin of dolomite and Precambrian seawater conditions as well as assisting in potential resolution of the enigmatic "dolomite problem".

6. Conclusions

A dataset of paired Mg/(Mg + Ca) and $\delta^{13}C_{carb}$ values for 991 well-preserved carbonate-rich samples were compiled from 17 sections containing part or all of the Shuram Excursion (SE) with a wide global distribution. The dolomite-dominated and calcite-dominated samples have $\delta^{13}C_{carb}$ values ranging from −10‰ to +7‰ and −10‰ to −5‰, respectively, whereas the mineralogically mixed samples exhibit a bimodal distribution with $\delta^{13}C_{carb}$ of either −10‰ to −5‰ or +4‰ to +8‰. Evaluating this dataset within the framework of known Ediacaran ocean chemistry and in the context of the recently proposed DOM catalyzation and large DOM reservoir hypotheses, we propose a new conceptual biogeochemical model for dolomite precipitation in the Ediacaran ocean featuring local DOM regulation of dolomite production. In this "DOM regulation model", a metastable DOM anaerobic oxidation zone existed between the oxic DOM-poor surface layer and the anoxic DOM-rich deep watermass. Within the DOM anaerobic oxidation zone, which operated most vigorously in shelf areas, DOM was oxidized by oxidants supplied by continental weathering fluxes, generating massive amounts of ^{13}C-depleted DIC. Calcite was precipitated under low-DOM conditions, which existed in oxic surface waters with $\delta^{13}C$ >+4‰ and the nearshore part of the DOM anaerobic oxidation zone with $\delta^{13}C$ ranging from +4‰ to −10‰, whereas dolomite was precipitated in high-DOM conditions, which existed in anoxic deep waters with $\delta^{13}C$ >+4‰ and the offshore part of the DOM anaerobic oxidation zone with $\delta^{13}C$ ranging from −10‰ to +4‰. The chemical conditions of formation of all samples are in line with our redox analyses. Our study highlights the possible linkage between massive dolomite precipitation and the existence of a large DOM reservoir in the redox-stratified Ediacaran ocean. Since the key boundary conditions in our model existed widely in early-Earth oceans, the DOM regulation model may provide a viable mechanism for deep-time massive dolomite precipitation that helps to resolve the enigmatic "dolomite problem". Finally, we note that our study is based on all available Ediacaran sections with relevant geochemical records, but more research will be needed to further explore the feasibility of our model of dolomite precipitation in other early oceans.

Declaration of Competing Interest

The authors declare that they have no known competing financial interests or personal relationships that could have appeared to influence the work reported in this paper.

Data availability

The data that has been used is included in this published article (and the Supplementary Data).

Acknowledgments

We thank Deng Liu, Xuan Qiu, Timothy Lyons, Bao Li, Biao Chang and Jun Hu for helpful discussions, we also thank two anonymous reviewers for their constructive comments. This study was supported by the NSFC (41825019, 42130208, 41821001, 42072335, 42050104, 41888101), the National Key Research and Development Program of China (2022YFF0800102) and 111 project of China (BP0820004).

Appendix A. Supplementary data

Supplementary data to this article can be found online at https://doi.org/10.1016/j.precamres.2022.106947.

References

Albert, D.B., Taylor, C., Martens, C.S., 1995. Sulfate reduction rates and low-molecular-weight fatty-acid concentrations in the water column and surficial sediments of the black-sea. Deep-Sea Res. Part I-Oceanogr. Res. Pap. 42, 1239–1260.

Al Disi, Z.A., Zouari, N., Attia, E., Al-Asali, M., Al-Kuwari, H.A.S., Sadooni, F., Dittrich, M., Bontognali, T.R.R., 2021. Systematic laboratory approach to produce Mg-rich carbonates at low temperature. RSC Adv. 11, 37029–37039.

Algeo, T.J., Li, C., 2020. Redox classification and calibration of redox thresholds in sedimentary systems. Geochim. Cosmochim. Acta 287, 8–26.

Algeo, T.J., Luo, G.M., Song, H.Y., Lyons, T.W., Canfield, D.E., 2015. Reconstruction of secular variation in seawater sulfate concentrations. Biogeosciences 12 (7), 2131–2151.

Baker, P.A., Kastner, M., 1981. Constraints on the formation of sedimentary dolomite. Science 213, 214–216.

Bar-On, Y.M., Phillips, R., Milo, R., 2018. The biomass distribution on Earth. Proc. Natl. Acad. Sci. 115 (25), 6506–6511.

Bau, M., Dulski, P., 1996. Distribution of yttrium and rare-earth elements in the Penge and Kuruman iron-formations, Transvaal Supergroup, South Africa. Precambr. Res. 79, 37–55.

Bau, M., Koschinsky, A., 2009. Oxidative scavenging of cerium on hydrous Fe oxide: Evidence from the distribution of rare earth elements and yttrium between Fe oxides and Mn oxides in hydrogenetic ferromanganese crusts. Geochem. J. 43, 37–47.
Bau, M., Moller, P., Dulski, P., 1997. Yttrium and lanthanides in eastern Mediterranean seawater and their fractionation during redox-cycling. Mar. Chem. 56, 123–131.
Berner, R.A., 1984. Sedimentary pyrite formation—an update. Geochim. Cosmochim. Acta 48, 605–615.
Burdett, J.W., Arthur, M.A., Richardson, M., 1989. A neogene seawater sulfur isotope age curve from calcareous pelagic microfossils. Earth Planet. Sci. Lett. 94, 189–198.
Burton, E.A., 1993. Controls on marine carbonate cement mineralogy: review and reassessment. Chem. Geol. 105, 163–179.
Busch, J.F., 2022. Stratigraphic Expression of the Ediacaran Shuram Carbon Isotope Excursion in Northwest Canada. Ph.D. dissertation, Dartmouth College, Hanover, New Hampshire, U.S.A.
Busch, J.F., Hodgin, E.B., Ahm, A.-S.-C., Husson, J.M., Macdonald, F.A., Bergmann, K.D., Higgins, J.A., Strauss, J.V., 2022. Global and local drivers of the Ediacaran Shuram carbon isotope excursion. Earth Planet. Sci. Lett. 579, 117368.
Cai, W.K., Liu, J.H., Zhou, C.H., Keeling, J., Glasmacher, U.A., 2021. Structure, genesis and resources efficiency of dolomite: New insights and remaining enigmas. Chem. Geol. 573, 120191.
Canfield, D.E., 2001. Isotope fractionation by natural populations of sulfate-reducing bacteria. Geochim. Cosmochim. Acta 65, 1117–1124.
Canfield, D.E., Thamdrup, B., 1994. The production of ^{34}S-depleted sulfide during bacterial disproportionation of elemental sulfur. Science 266, 1973–1975.
Canfield, D.E., Farquhar, J., Zerkle, A.L., 2010. High isotope fractionations during sulfate reduction in a low-sulfate euxinic ocean analog. Geology 38, 415–418.
Cantine, M.D., Knoll, A.H., Bergmann, K.D., 2020. Carbonates before skeletons: A database approach. Earth Sci. Rev. 201, 103065.
Cao, M., Daines, S.J., Lenton, T.M., Cui, H., Algeo, T.J., Dahl, T.W., Shi, W., Chen, Z.-Q., Anbar, A., Zhou, Y.-Q., 2020. Comparison of Ediacaran platform and slope δ ^{238}U records in South China: Implications for global-ocean oxygenation and the origin of the Shuram Excursion. Geochim. Cosmochim. Acta 287, 111–124.
Chance, R., Baker, A.R., Carpenter, L., Jickells, T.D., 2014. The distribution of iodide at the sea surface. Environ. Sci.—Processes Impacts 16, 1841–1859.
Chang, B., Li, C., Liu, D., Foster, I., Tripati, A., Lloyd, M.K., Maradiaga, I., Luo, G., An, Z., She, Z., Xie, S., Tong, J., Huang, J., Algeo, T.J., Lyons, T.W., Immenhauser, A., 2020. Massive formation of early diagenetic dolomite in the Ediacaran ocean: Constraints on the "dolomite problem". Proceedings of the National Academy of Sciences (U.S. A.) 117, 14005-14014.
Chen, B., Hu, C., Mills, B.J.W., He, T., Andersen, M.B., Chen, X., Liu, P., Lu, M., Newton, R.J., Poulton, S.W., Shields, G.A., Zhu, M., 2022. A short-lived oxidation event during the early Ediacaran and delayed oxygenation of the Proterozoic ocean. Earth Planet. Sci. Lett. 577, 117274.
Chen, X., Ling, H.-F., Vance, D., Shields-Zhou, G.A., Zhu, M., Poulton, S.W., Och, L.M., Jiang, S.-Y., Li, D., Cremonese, L., Archer, C., 2015. Rise to modern levels of ocean oxygenation coincided with the Cambrian radiation of animals. Nat. Commun. 6, 1–7.
Ciais, P., Sabine, C., Bala, G., Bopp, L., Brovkin, V., Canadell, J., Chhabra, A., DeFries, R., Galloway, J., Heimann, M., Jones, C., Le Quéré, C., Myneni, R.B., Piao, S., Thornton, P., 2013. Carbon and other biogeochemical cycles. In: Stocker, T.F. (Ed.), Climate change 2013: The physical science basis. Contribution of Working Group I to the Fifth Assessment Report of the Intergovernmental Panel on Climate Change. Cambridge University Press, Cambridge, United Kingdom and New York, NY, USA, pp. 465–570.
Condon, D., Zhu, M.Y., Bowring, S., Wang, W., Yang, A.H., Jin, Y.G., 2005. U-Pb ages from the Neoproterozoic Doushantuo Formation, China. Science 308, 95–98.
Dahl, T.W., Hammarlund, E.U., Anbar, A.D., Bond, D.P.G., Gill, B.C., Gordon, G.W., Knoll, A.H., Nielsen, A.T., Schovsbo, N.H., Canfield, D.E., 2010. Devonian rise in atmospheric oxygen correlated to the radiations of terrestrial plants and large predatory fish. Proceedings of the National Academy of Sciences (U.S.A.) 107, 17911-17915.
Debaar, H.J.W., Bacon, M.P., Brewer, P.G., Bruland, K.W., 1985. Rare-earth elements in the Pacific and Atlantic oceans. Geochim. Cosmochim. Acta 49, 1943–1959.
Debaar, H.J.W., German, C.R., Elderfield, H., Vangaans, P., 1988. Rare-earth element distributions in anoxic waters of the Cariaco Trench. Geochim. Cosmochim. Acta 52, 1203–1219.
Dedeckker, P., Last, W.M., 1988. Modern dolomite deposition in continental, saline lakes, western Victoria, Australia. Geology 16, 29–32.
Du, Y., Fan, T., Machel, H.G., Gao, Z., 2018. Genesis of Upper Cambrian-Lower Ordovician dolomites in the Tahe Oilfield, Tarim Basin, NW China: Several limitations from petrology, geochemistry, and fluid inclusions. Mar. Pet. Geol. 91, 43–70.
Ducklow, H.W., Hansell, D.A., Morgan, J.A., 2007. Dissolved organic carbon and nitrogen in the Western Black Sea. Mar. Chem. 105, 140–150.
Emerson, S., Cranston, R., Liss, P., 1979. Redox species in a reducing fjord: equilibrium and kinetic considerations. Deep Sea Research Part A. Oceanographic Res. Papers 26, 859–878.
Fairbridge, R.W., 1957. The dolomite question. In Le Blanc, R.J., Breeding, J.G. (eds.), Regional Aspects of Carbonate Deposition, SEPM Special Publication No. 5, pp. 125-178.
Fan, H., Zhu, X., Wen, H., Yan, B., Li, J., Feng, L., 2014. Oxygenation of Ediacaran Ocean recorded by iron isotopes. Geochim. Cosmochim. Acta 140, 80–94.
Fang, Y., Xu, H., 2019. A new approach to quantify the ordering state of protodolomite using XRD, TEM, and Z-contrast imaging. J. Sediment. Res. 89, 537–551.
Fang, Y., Zhang, F., Farfan, G.A., Xu, H., 2022. Low-temperature synthesis of disordered dolomite and high-magnesium calcite in ethanol-water solutions: The solvation effect and implications. ACS Omega 7, 281–292.
Farquhar, G.D., Ehleringer, J.R., Hubick, K.T., 1989. Carbon isotope discrimination and photosynthesis. Annu. Rev. Plant. Physiol. Plant. Mol. Biol. 40, 503–537.
Fike, D.A., Grotzinger, J.P., Pratt, L.M., Summons, R.E., 2006. Oxidation of the Ediacaran Ocean. Nature 444, 744–747.
Gao, Y., Zhang, X., Zhang, G., Chen, K., Shen, Y., 2018. Ediacaran negative C-isotopic excursions associated with phosphogenic events: Evidence from South China. Precambr. Res. 307, 218–228.
Garaguly, I., Varga, A., Raucsik, B., Schubert, F., Czuppon, G., Frei, R., 2018. Pervasive early diagenetic dolomitization, subsequent hydrothermal alteration, and late stage hydrocarbon accumulation in a Middle Triassic carbonate sequence (Szeged Basin, SE Hungary). Mar. Petrol. Geol. 98, 270–290.
German, C.R., Holliday, B.P., Elderfield, H., 1991. Redox cycling of rare-earth elements in the suboxic zone of the Black Sea. Geochim. Cosmochim. Acta 55, 3553–3558.
Glock, N., Liebetrau, V., Eisenhauer, A., 2014. I/Ca ratios in benthic foraminifera from the Peruvian oxygen minimum zone: Analytical methodology and evaluation as a proxy for redox conditions. Biogeosciences 11, 7077–7095.
Gomez-Saez, G.V., Dittmar, T., Holtappels, M., Pohlabeln, A.M., Lichtschlag, A., Schnetger, B., Boetius, A., Niggemann, J., 2021. Sulfurization of dissolved organic matter in the anoxic water column of the Black Sea. Science. Advances 7 (25), eabf6199.
Gregg, J.M., Bish, D.L., Kaczmarek, S.E., Machel, H.G., 2015. Mineralogy, nucleation and growth of dolomite in the laboratory and sedimentary environment: A review. Sedimentology 62, 1749–1769.
Grotzinger, J.P., Knoll, A.H., 1995. Anomalous carbonate precipitates: Is the Precambrian the key to the Permian? PALAIOS 10, 578–596.
Grotzinger, J.P., Fike, D.A., Fischer, W.W., 2011. Enigmatic origin of the largest-known carbon isotope excursion in Earth's history. Nat. Geosci. 4, 285–292.
Hansell, D.A., 2013. Recalcitrant dissolved organic carbon fractions, *in*: Carlson, C.A., Giovannoni, S.J. (Eds.), Annual Review of Marine Science, vol. 5, pp. 421-445.
Hansell, D.A., Carlson, C.A., Repeta, D.J., Schlitzer, R., 2009. Dissolved organic matter in the ocean a controversy stimulates new insights. Oceanography 22, 202–211.
Hardisty, D.S., Lu, Z., Bekker, A., Diamond, C.W., Gill, B.C., Jiang, G., Kah, L.C., Knoll, A. H., Loyd, S.J., Osburn, M.R., Planavsky, N.J., Wang, C., Zhou, X., Lyons, T.W., 2017. Perspectives on Proterozoic surface ocean redox from iodine contents in ancient and recent carbonate. Earth Planet. Sci. Lett. 463, 159–170.
Hayes, J.M., Strauss, H., Kaufman, A.J., 1999. The abundance of ^{13}C in marine organic matter and isotopic fractionation in the global biogeochemical cycle of carbon during the past 800 Ma. Chem. Geol. 161, 103–125.
Hertkorn, N., Benner, R., Frommberger, M., Schmitt-Kopplin, P., Witt, M., Kaiser, K., Kettrup, A., Hedges, J.I., 2006. Characterization of a major refractory component of marine dissolved organic matter. Geochim. Cosmochim. Acta 70, 2990–3010.
Higgins, J.A., Schrag, D.P., 2003. Aftermath of a snowball Earth. Geochem. Geophys. Geosyst. 4 (3).
Huang, K.-J., Shen, B., Lang, X.-G., Tang, W.-B., Peng, Y., Ke, S., Kaufman, A.J., Ma, H.-R., Li, F.-B., 2015. Magnesium isotopic compositions of the Mesoproterozoic dolostones: Implications for Mg isotopic systematics of marine carbonates. Geochim. Cosmochim. Acta 164, 333–351.
Hoffman, P.F., Kaufman, A.J., Halverson, G.P., Schrag, D.P., 1998. A Neoproterozoic snowball earth. Science 281, 1342–1346.
Holland, H.D., Zimmerman, H., 2000. The dolomite problem revisited. Int. Geol. Rev. 42, 481–490.
Hsü, K.J., 1966. Origin of dolomite in sedimentary sequences: a critical analysis. Miner. Deposita 1, 133–138.
Hurtgen, M.T., Arthur, M.A., Halverson, G.P., 2005. Neoproterozoic sulfur isotopes, the evolution of microbial sulfur species, and the burial efficiency of sulfide as sedimentary pyrite. Geology 33, 41–44.
James, N.P., Narbonne, G.M., Kyser, T.K., 2001. Late Neoproterozoic cap carbonates: Mackenzie Mountains, northwestern Canada: precipitation and global glacial meltdown. Can. J. Earth Sci. 38, 1229–1262.
Jiang, G., Kennedy, M.J., Christie-Blick, N., 2003. Stable isotopic evidence for methane seeps in Neoproterozoic postglacial cap carbonates. Nature 426, 822–826.
Jiang, G., Kaufman, A.J., Christie-Blick, N., Zhang, S., Wu, H., 2007. Carbon isotope variability across the Ediacaran Yangtze platform in South China: Implications for a large surface-to-deep ocean δ ^{13}C gradient. Earth Planet. Sci. Lett. 261, 303–320.
Jiang, G., Shi, X., Zhang, S., Wang, Y., Xiao, S., 2011. Stratigraphy and paleogeography of the Ediacaran Doushantuo Formation (ca. 635–551 Ma) in South China. Gondw. Res. 19, 831–849.
Jiang, G., Wang, X., Shi, X., Xiao, S., Zhang, S., Dong, J., 2012. The origin of decoupled carbonate and organic carbon isotope signatures in the early Cambrian (ca. 542–520 Ma) Yangtze platform. Earth Planet. Sci. Lett. 317, 96–110.
Jiao, N., Herndl, G.J., Hansell, D.A., Benner, R., Kattner, G., Wilhelm, S.W., Kirchman, D. L., Weinbauer, M.G., Luo, T., Chen, F., Azam, F., 2010. Microbial production of recalcitrant dissolved organic matter: long-term carbon storage in the global ocean. Nat. Rev. Microbiol. 8, 593–599.
Kah, L.C., Lyons, T.W., Frank, T.D., 2004. Low marine sulphate and protracted oxygenation of the Proterozoic biosphere. Nature 431, 834–838.
Kampschulte, A., Strauss, H., 2004. The sulfur isotopic evolution of Phanerozoic seawater based on the analysis of structurally substituted sulfate in carbonates. Chem. Geol. 204, 255–286.
Kampschulte, A., Bruckschen, P., Strauss, H., 2001. The sulphur isotopic composition of trace sulphates in Carboniferous brachiopods: implications for coeval seawater, correlation with other geochemical cycles and isotope stratigraphy. Chem. Geol. 175, 149–173.

Kasten, S., Jørgensen, B.B., 2000. Sulfate reduction in marine sediments, In: Marine Geochemistry. Schulz H.D., Zabel, M., (eds). Springer Berlin Heidelberg, Berlin, Heidelberg, p 263–281.Kaufman, A.J., Knoll, A.H., 1995. Neoproterozoic variations in the C-isotopic composition of seawater—stratigraphic and biogeochemical implications. Precambrian Research 73, 27-49.
Kaufman, A.J., Knoll, A.H., 1995. Neoproterozoic variations in the C-isotopic composition of seawater: stratigraphic and biogeochemical implications. Precambr. Res. 73, 27–49.
Kazmierczak, J., Kempe, S., Kremer, B., 2013. Calcium in the early evolution of living systems: A biohistorical approach. Curr. Org. Chem. 17, 1738–1750.
Keil, R., Annual, R., 2017. Anthropogenic forcing of carbonate and organic carbon preservation in marine sediments. Ann. Rev. Mar. Sci. 9, 151–172.
Kendall, B., Komiya, T., Lyons, T.W., Bates, S.M., Gordon, G.W., Romaniello, S.J., Jiang, G., Creaser, R.A., Xiao, S., McFadden, K., Sawaki, Y., Tahata, M., Shu, D., Han, J., Li, Y., Chu, X., Anbar, A.D., 2015. Uranium and molybdenum isotope evidence for an episode of widespread ocean oxygenation during the late Ediacaran Period. Geochim. Cosmochim. Acta 156, 173–193.
Kennedy, M.J., Christie-Blick, N., 2011. Condensation origin for Neoproterozoic cap carbonates during deglaciation. Geology 39, 319–322.
Kennedy, M.J., Christie-Blick, N., Sohl, L.E., 2001. Are Proterozoic cap carbonates and isotopic excursions a record of gas hydrate destabilization following Earth's coldest intervals? Geology 29, 443–446.
Kenward, P.A., Fowle, D.A., Goldstein, R.H., Ueshima, M., Gonzalez, L.A., Roberts, J.A., 2013. Ordered low-temperature dolomite mediated by carboxyl-group density of microbial cell walls. AAPG Bull. 97, 2113–2125.
Knauth, L.P., Kennedy, M.J., 2009. The late Precambrian greening of the Earth. Nature 460, 728–732.
Kump, L.R., 1991. Interpreting carbon-isotope excursions: Strangelove oceans. Geology 19 (4), 299–302.
Land, L.S., 1998. Failure to precipitate dolomite at 25 °C from dilute solution despite 1000-fold oversaturation after 32 years. Aquat. Geochem. 4 (3), 361–368.
Lawrence, M.G., Greig, A., Collerson, K.D., Kamber, B.S., 2006. Rare earth element and yttrium variability in south east Queensland waterways. Aquat. Geochem. 12, 39–72.
Li, C., Love, G.D., Lyons, T.W., Fike, D.A., Sessions, A.L., Chu, X., 2010. A stratified redox model for the Ediacaran ocean. Science 328, 80–83.
Li, C., Hardisty, D.S., Luo, G., Huang, J., Algeo, T.J., Cheng, M., Shi, W., An, Z., Tong, J., Xie, S., Jiao, N., Lyons, T.W., 2017. Uncovering the spatial heterogeneity of Ediacaran carbon cycling. Geobiology 15, 211–224.
Li, C., Cheng, M., Zhu, M., Lyons, T.W., 2018. Heterogeneous and dynamic marine shelf oxygenation and coupled early animal evolution. Emerging Top. Life Sci. 2, 279–288.
Li, C., Shi, W., Cheng, M., Jin, C., Algeo, T.J., 2020a. The redox structure of Ediacaran and early Cambrian oceans and its controls. Sci. Bull. 65, 2141–2149.
Li, N., Zhang, F., Gao, J., Cao, M., Wei, G.-Y., Wang, H., Zhang, Z., Cheng, M., Xiong, G., Zhou, J., 2022. Assessing bulk carbonates as archives for seawater sulfur isotopic composition using shallow water cores from the South China Sea. Palaeogeogr. Palaeoclimatol. Palaeoecol. 598, 111029.
Li, Z., Cao, M., Loyd, S.J., Algeo, T.J., Zhao, H., Wang, X., Zhao, L., Chen, Z.-Q., 2020b. Transient and stepwise ocean oxygenation during the late Ediacaran Shuram Excursion: Insights from carbonate δ ^{238}U of northwestern Mexico. Precambr. Res. 344, 105741.
Ling, H.-F., Chen, X., Li, D., Wang, D., Shields-Zhou, G.A., Zhu, M., 2013. Cerium anomaly variations in Ediacaran-earliest Cambrian carbonates from the Yangtze Gorges area, South China: Implications for oxygenation of coeval shallow seawater. Precambr. Res. 225, 110–127.
Lippmann, F., 1982. Stable and metastable solubility diagrams for the system $CaCO_3$ - $MgCO_3$ - H_2O at ordinary temperature. Bull. Minér. 105, 273–279.
Liu, D., Yu, N., Papineau, D., Fan, Q., Wang, H., Qiu, X., She, Z., Luo, G., 2019. The catalytic role of planktonic aerobic heterotrophic bacteria in protodolomite formation: Results from Lake Jibuhulangtu Nuur, Inner Mongolia, China. Geochim. Cosmochim. Acta 263, 31–49.
Liu, D., Xu, Y., Yu, Q., Yu, N., Qiu, X., Wang, H., Papineau, D., 2020. Catalytic effect of microbially-derived carboxylic acids on the precipitation of Mg-calcite and disordered dolomite: Implications for sedimentary dolomite formation. J. Asian Earth Sci. 193, 104301.
Logan, G.A., Hayes, J.M., Hieshima, G.B., Summons, R.E., 1995. Terminal Proterozoic reorganization of biogeochemical cycles. Nature 376, 53–56.
Loyd, S.J., Berelson, W.M., Lyons, T.W., Hammond, D.E., Corsetti, F.A., 2012a. Constraining pathways of microbial mediation for carbonate concretions of the Miocene Monterey Formation using carbonate-associated sulfate. Geochim. Cosmochim. Acta 78, 77–98.
Loyd, S.J., Marenco, P.J., Hagadorn, J.W., Lyons, T.W., Kaufman, A.J., Sour-Tovar, F., Corsetti, F.A., 2012b. Sustained low marine sulfate concentrations from the Neoproterozoic to the Cambrian: Insights from carbonates of northwestern Mexico and eastern California. Earth Planet. Sci. Lett. 339, 79–94.
Loyd, S.J., Marenco, P.J., Hagadorn, J.W., Lyons, T.W., Kaufman, A.J., Sour-Tovar, F., Corsetti, F.A., 2013. Local δ ^{34}S variability in ~580 Ma carbonates of northwestern Mexico and the Neoproterozoic marine sulfate reservoir. Precambr. Res. 224, 551–569.
Lu, Z., Jenkyns, H.C., Rickaby, R.E.M., 2010. Iodine to calcium ratios in marine carbonate as a paleo-redox proxy during oceanic anoxic events. Geology 38, 1107–1110.
Lu, Z., Hoogakker, B.A.A., Hillenbrand, C.-D., Zhou, X., Thomas, E., Gutchess, K.M., Lu, W., Jones, L., Rickaby, R.E.M., 2016. Oxygen depletion recorded in upper waters of the glacial Southern Ocean. Nat. Commun. 7, 11146.
Lv, Y., Liu, S.-A., Wu, H., Hohl, S.V., Chen, S., Li, S., 2018. Zn-Sr isotope records of the Ediacaran Doushantuo Formation in South China: diagenesis assessment and implications. Geochim. Cosmochim. Acta 239, 330–345.
Lyons, T.W., Reinhard, C.T., Planavsky, N.J., 2014. The rise of oxygen in Earth's early ocean and atmosphere. Nature 506, 307–315.
Lyons, T.W., Diamond, C.W., Planavsky, N.J., Reinhard, C.T., Li, C., 2021. Oxygenation, life, and the planetary system during Earth's middle history: An Overview. Astrobiology 21, 906–923.
Machel, H.G., 2004. Concepts and models of dolomitization: a critical reappraisal. Geological Society, London, Special Publication 235, 7–63.
McFadden, K.A., Huang, J., Chu, X., Jiang, G., Kaufman, A.J., Zhou, C., Yuan, X., Xiao, S., 2008. Pulsed oxidation and bioloical evolution in the Ediacaran Doushantuo Formation. Proceedings of the National Academy of Sciences (U.S.A.) 105, 3197-3202.
McKenzie, J.A., Vasconcelos, C., 2009. Dolomite Mountains and the origin of the dolomite rock of which they mainly consist: historical developments and new perspectives. Sedimentology 56, 205–219.
McLennan, S.M., 1989. Rare earth elements in sedimentary rocks: influence of provenance and sedimentary processes, Geochemistry and Mineralogy of Rare Earth Elements. De Gruyter 169–200.
Melezhik, V.A., Pokrovsky, B.G., Fallick, A.E., Kuznetsov, A.B., Bujakaite, M.I., 2009. Constraints on $^{87}Sr/^{86}Sr$ of Late Ediacaran seawater: Insight from Siberian high-Sr limestones. J. Geol. Soc. Lond. 166, 183–191.
Merdith, A.S., Collins, A.S., Williams, S.E., Pisarevsky, S., Foden, J.D., Archibald, D.B., Blades, M.L., Alessio, B.L., Armistead, S., Plavsa, D., 2017. A full-plate global reconstruction of the Neoproterozoic. Gondw. Res. 50, 84–134.
Michard, A., Albarede, F., 1986. The REE content of some hydrothermal fluids. Chem. Geol. 55, 51–60.
Mucci, A., Morse, J.W., 1983. The incorporation of Mg^{2+} and Sr^{2+} into calcite overgrowths—influences of growth-rate and solution composition. Geochim. Cosmochim. Acta 47, 217–233.
Nagata, T., Fukuda, H., Fukuda, R., Koike, I., 2000. Bacterioplankton distribution and production in deep Pacific waters: Large-scale geographic variations and possible coupling with sinking particle fluxes. Limnol. Oceanogr. 45, 426–435.
Nelson, C.S., 1988. An introductory perspective on non-tropical shelf carbonates. Sed. Geol. 60, 3–12.
Ngia, N.R., Hu, M., Gao, D., 2019. Tectonic and geothermal controls on dolomitization and dolomitizing fluid flows in the Cambrian-Lower Ordovician carbonate successions in the western and central Tarim Basin, NW China. J. Asian Earth Sci. 172, 359–382.
Nordeng, S.H., Sibley, D.F., 1994. Dolomite stoichiometry and Ostwald's step rule. Geochim. Cosmochim. Acta 58, 191–196.
Osburn, M.R., 2013. Isotopic proxies for microbial and environmental change: insights from hydrogen isotopes and the Ediacaran Khufai Formation. California Institute of Technology, Pasadena, California. Ph.D. dissertation,.
Osburn, M.R., Owens, J., Bergmann, K.D., Lyons, T.W., Grotzinger, J.P., 2015. Dynamic changes in sulfate sulfur isotopes preceding the Ediacaran Shuram Excursion. Geochim. Cosmochim. Acta 170, 204–224.
Petrash, D.A., Bialik, O.M., Bontognali, T.R., Vasconcelos, C., Roberts, J.A., McKenzie, J. A., Konhauser, K.O., 2017. Microbially catalyzed dolomite formation: from near-surface to burial. Earth Sci. Rev. 171, 558–582.
Pina, C.M., Pimentel, C., Crespo, Á., 2022. The Dolomite Problem: A matter of time. ACS Earth Space Chem. 6, 1468–1471.
Poulton, S.W., Canfield, D.E., 2011. Ferruginous conditions: A dominant feature of the ocean through Earth's history. Elements 7, 107–112.
Qiu, X., Wang, H., Yao, Y., Duan, Y., 2017. High salinity facilitates dolomite precipitation mediated by *Haloferax volcanii* DS52. Earth Planet. Sci. Lett. 472, 197–205.
Reinhard, C.T., Planavsky, N.J., Olson, S.L., Lyons, T.W., Erwin, D.H., 2016. Earth's oxygen cycle and the evolution of animal life. Proceedings of the National Academy of Sciences (U.S.A.) 113, 8933-8938.
Rennie, V.C.F., Turchyn, A.V., 2014. The preservation of δ $^{34}S_{SO4}$ and δ $^{18}O_{SO4}$ in carbonate-associated sulfate during marine diagenesis: A 25 Myr test case using marine sediments. Earth Planet. Sci. Lett. 395, 13–23.
Ridgwell, A., Arndt, S., 2015. Why dissolved organics matter: DOC in ancient oceans and past climate change, Biogeochemistry of marine dissolved organic matter. Elsevier, pp. 1-20.
Ridgwell, A., Zeebe, R.E., 2005. The role of the global carbonate cycle in the regulation and evolution of the Earth system. Earth Planet. Sci. Lett. 234, 299–315.
Roberts, J.A., Kenward, P.A., Fowle, D.A., Goldstein, R.H., Gonzalez, L.A., Moore, D.S., 2013. Surface chemistry allows for abiotic precipitation of dolomite at low temperature. Proceedings of the National Academy of Sciences (U.S.A.) 110, 14540-14545.
Rothman, D.H., Hayes, J.M., Summons, R.E., 2003. Dynamics of the Neoproterozoic carbon cycle. Proceedings of the National Academy of Sciences (U.S.A.) 100, 8124-8129.
Rue, E.L., Smith, G.J., Cutter, G.A., Bruland, K.W., 1997. The response of trace element redox couples to suboxic conditions in the water column. Deep-Sea Res. Part I-Oceanogr. Res. Pap. 44, 113–134.
Sahoo, S.K., Planavsky, N.J., Jiang, G., Kendall, B., Owens, J.D., Wang, X., Shi, X., Anbar, A.D., Lyons, T.W., 2016. Oceanic oxygenation events in the anoxic Ediacaran ocean. Geobiology 14, 457–468.
Shen, Z., Liu, Y., Brown, P.E., Szlufarska, I., Xu, H., 2014. Modeling the effect of dissolved hydrogen sulfide on Mg2+-water complex on dolomite 104 surfaces. J. Phys. Chem. C 118, 15716–15722.

Shen, Z., Szlufarska, I., Brown, P.E., Xu, H., 2015. Investigation of the role of polysaccharide in the dolomite growth at low temperature by using atomistic simulations. Langmuir 31, 10435–10442.
Shi, W., Li, C., Luo, G., Huang, J., Algeo, T.J., Jin, C., Zhang, Z., Cheng, M., 2018. Sulfur isotope evidence for transient marine-shelf oxidation during the Ediacaran Shuram Excursion. Geology 46, 267–270.
Shields, G.A., 2005. Neoproterozoic cap carbonates: a critical appraisal of existing models and the plumeworld hypothesis. Terra Nova 17, 299–310.
Shields, G.A., Mills, B.J.W., Zhu, M., Raub, T.D., Daines, S.J., Lenton, T.M., 2019. Unique Neoproterozoic carbon isotope excursions sustained by coupled evaporite dissolution and pyrite burial. Nat. Geosci. 12, 823–827.
Sholkovitz, E.R., Landing, W.M., Lewis, B.L., 1994. Ocean particle chemistry—the fractionation of rare-earth elements between suspended particles and seawater. Geochim. Cosmochim. Acta 58, 1567–1579.
Slack, J.F., Grenne, T., Bekker, A., Rouxel, O.J., Lindberg, P.A., 2007. Suboxic deep seawater in the late Paleoproterozoic: Evidence from hematitic chert and iron formation related to seafloor-hydrothermal sulfide deposits, central Arizona, USA. Earth Planet. Sci. Lett. 255, 243–256.
Sperling, E.A., Wolock, C.J., Morgan, A.S., Gill, B.C., Kunzmann, M., Halverson, G.P., Macdonald, F.A., Knoll, A.H., Johnston, D.T., 2015. Statistical analysis of iron geochemical data suggests limited late Proterozoic oxygenation. Nature 523, 451–454.
Stephenson, A.E., DeYoreo, J.J., Wu, L., Wu, K.J., Hoyer, J., Dove, P.M., 2008. Peptides enhance magnesium signature in calcite: Insights into origins of vital effects. Science 322, 724–727.
Stewart, J.H., McMenamin, M.A., Morales-Ramirez, J., 1984. Upper Proterozoic and Cambrian rocks in the Caborca region. Sonora, Mexico—Physical stratigraphy, biostratigraphy, paleocurrent studies, and regional relations. U.S. Geol. Surv. Prof. Pap. 1309, 36 pp.
Stolper, D.A., Bucholz, C.E., 2019. Neoproterozoic to early Phanerozoic rise in island arc redox state due to deep ocean oxygenation and increased marine sulfate levels. Proceedings of the National Academy of Sciences (U.S.A.) 116, 8746-8755.
Stolper, D.A., Keller, C.B., 2018. A record of deep-ocean dissolved O_2 from the oxidation state of iron in submarine basalts. Nature 553, 323–327.
Swanson-Hysell, N.L., Rose, C.V., Calmet, C.C., Halverson, G.P., Hurtgen, M.T., Maloof, A.C., 2010. Cryogenian glaciation and the onset of carbon-isotope decoupling. Science 328, 608–611.
Toroz, D., Song, F., Chass, G.A., Di Tommaso, D., 2021. New insights into the role of solution additive anions in Mg^{2+} dehydration: Implications for mineral carbonation. CrstEngComm 23, 4896–4900.
Tostevin, R., Shields, G.A., Tarbuck, G.M., He, T., Clarkson, M.O., Wood, R.A., 2016a. Effective use of cerium anomalies as a redox proxy in carbonate-dominated marine settings. Chem. Geol. 438, 146–162.
Tostevin, R., Wood, R.A., Shields, G.A., Poulton, S.W., Guilbaud, R., Bowyer, F., Penny, A.M., He, T., Curtis, A., Hoffmann, K.H., Clarkson, M.O., 2016b. Low-oxygen waters limited habitable space for early animals. Nat. Commun. 7, 12818.
Tucker, M.E., Wright, V.P., 1990. Carbonate Sedimentology. Blackwell Scientific Publications, London, U.K., pp. 284–362 (Ch. 6–7).
Urosevic, M., Rodriguez-Navarro, C., Putnis, C.V., Cardell, C., Putnis, A., Ruiz-Agudo, E., 2012. In situ nanoscale observations of the dissolution of 10¯14 dolomite cleavage surfaces. Geochim. Cosmochim. Acta 80, 1–13.
Van Cappellen, P., Ingall, E.D., 1994. Benthic phosphorus regeneration, net primary production, and ocean anoxia—A model of the coupled marine biogeochemical cycles of carbon and phosphorus. Paleoceanography 9, 677–692.
Vasconcelos, C., McKenzie, J.A., 1997. Microbial mediation of modern dolomite precipitation and diagenesis under anoxic conditions (Lagoa Vermelha, Rio de Janeiro, Brazil). J. Sediment. Res. 67, 378–390.
Wang, J., Jiang, G., Xiao, S., Li, Q., Wei, Q., 2008. Carbon isotope evidence for widespread methane seeps in the ca. 635 Ma Doushantuo cap carbonate in south China. Geology 36, 347–350.
Wang, J., He, Z., Zhu, D., Liu, Q., Ding, Q., Li, S., Zhang, D., 2020. Petrological and geochemical characteristics of the botryoidal dolomite of Dengying Formation in the Yangtze Craton, South China: Constraints on terminal Ediacaran "dolomite seas". Sed. Geol. 406, 105722.
Wang, X., Chou, I.M., Hu, W., Yuan, S., Liu, H., Wan, Y., Wang, X., 2016a. Kinetic inhibition of dolomite precipitation: Insights from Raman spectroscopy of Mg^{2+} – SO2- 4 ion pairing in $MgSO_4/MgCl_2$/NaCl solutions at temperatures of 25 to 200 °C. Chem. Geol. 435, 10–21.
Wang, X., Jiang, G., Shi, X., Xiao, S., 2016b. Paired carbonate and organic carbon isotope variations of the Ediacaran Doushantuo Formation from an upper slope section at Siduping, South China. Precambr. Res. 273, 53–66.
Wang, Z., Wang, J., Kouketsu, Y., Bodnar, R.J., Gill, B.C., Xiao, S., 2017. Raman geothermometry of carbonaceous material in the basal Ediacaran Doushantuo cap dolostone: The thermal history of extremely negative δ ^{13}C signatures in the aftermath of the terminal Cryogenian snowball Earth glaciation. Precambr. Res. 298, 174–186.
Warren, J., 2000. Dolomite: occurrence, evolution and economically important associations. Earth Sci. Rev. 52, 1–81.
Warthmann, R., van Lith, Y., Vasconcelos, C., McKenzie, J.A., Karpoff, A.M., 2000. Bacterially induced dolomite precipitation in anoxic culture experiments. Geology 28, 1091–1094.
Webb, G.E., Kamber, B.S., 2000. Rare earth elements in Holocene reefal microbialites: A new shallow seawater proxy. Geochim. Cosmochim. Acta 64, 1557–1565.
Wei, G.-Y., Hood, A.v.S., Chen, X., Li, D., Wei, W., Wen, B., Gong, Z., Yang, T., Zhang, Z.-F., Ling, H.-F., 2019a. Ca and Sr isotope constraints on the formation of the Marinoan cap dolostones. Earth and Planetary Science Letters 511, 202-212.
Wei, H., Wang, X., Shi, X., Jiang, G., Tang, D., Wang, L., An, Z., 2019. Iodine content of the carbonates from the Doushantuo Formation and shallow ocean redox change on the Ediacaran Yangtze Platform, South China. Precambr. Res. 322, 160–169.
Wei, W., Frei, R., Gilleaudeau, G.J., Li, D., Wei, G.-Y., Chen, X., Ling, H.-F., 2018. Oxygenation variations in the atmosphere and shallow seawaters of the Yangtze Platform during the Ediacaran Period: Clues from Cr-isotope and Ce-anomaly in carbonates. Precambr. Res. 313, 78–90.
Wong, G., Brewer, P.G., 1977. The marine chemistry of iodine in anoxic basins. Geochim. Cosmochim. Acta 41, 151–159.
Wood, R.A., Zhuravlev, A.Y., Sukhov, S.S., Zhu, M., Zhao, F., 2017. Demise of Ediacaran dolomitic seas marks widespread biomineralization on the Siberian Platform. Geology 45, 27–30.
Wright, D.T., 1999. The role of sulphate-reducing bacteria and cyanobacteria in dolomite formation in distal ephemeral lakes of the Coorong region, South Australia. Sed. Geol. 126, 147–157.
Xing, C., Liu, P., Wang, R., Li, C., Li, J., Shen, B., 2022. Tracing the evolution of dissolved organic carbon (DOC) pool in the Ediacaran ocean by germanium/silica (Ge/Si) ratios of diagenetic chert nodules from the Doushantuo Formation. South China. Precambrian Research 374, 106639.
Zhang, C., Dang, H., Azam, F., Benner, R., Legendre, L., Passow, U., Polimene, L., Robinson, C., Suttle, C.A., Jiao, N., 2018. Evolving paradigms in biological carbon cycling in the ocean. Natl. Sci. Rev. 5, 481–499.
Zhang, F., Xu, H., Konishi, H., Kemp, J.M., Roden, E.E., Shen, Z., 2012a. Dissolved sulfide-catalyzed precipitation of disordered dolomite: Implications for the formation mechanism of sedimentary dolomite. Geochim. Cosmochim. Acta 97, 148–165.
Zhang, F., Xu, H., Konishi, H., Shelobolina, E.S., Roden, E.E., 2012b. Polysaccharide-catalyzed nucleation and growth of disordered dolomite: A potential precursor of sedimentary dolomite. Am. Mineral. 97, 556–567.
Zhang, F., Xiao, S., Romaniello, S.J., Hardisty, D., Li, C., Melezhik, V., Pokrovsky, B., Cheng, M., Shi, W., Lenton, T.M., Anbar, A.D., 2019. Global marine redox changes drove the rise and fall of the Ediacara biota. Geobiology 17, 594–610.
Zhang, F., Xu, H., Shelobolina, E.S., Konishi, H., Roden, E.E., 2021. Precipitation of low-temperature disordered dolomite induced by extracellular polymeric substances of methanogenic Archaea *Methanosarcina barkeri*: Implications for sedimentary dolomite formation. Am. Mineral. 106, 69–81.
Zhang, K., Shields, G.A., 2022. Sedimentary Ce anomalies: Secular change and implications for paleoenvironmental evolution. Earth Sci. Rev. 229, 104015.
Zhong, S.J., Mucci, A., 1995. Partitioning of rare-earth elements (REEs) between calcite and seawater solutions at 25°C and 1 atm, and high dissolved REE concentrations. Geochim. Cosmochim. Acta 59, 443–453.
Zhou, C., Jiang, S., Xiao, S., Chen, Z., Yuan, X., 2012. Rare earth elements and carbon isotope geochemistry of the Doushantuo Formation in South China: Implication for middle Ediacaran shallow marine redox conditions. Chin. Sci. Bull. 57, 1998–2006.
Zhu, M., Zhang, J., Yang, A., 2007. Integrated Ediacaran (Sinian) chronostratigraphy of South China. Palaeogeogr. Palaeoclimatol. Palaeoecol. 254, 7–61.